Journal of Structural Geology 34 (2012) 2–19

Contents lists available at SciVerse ScienceDirect

Journal of Structural Geology

journal homepage: www.elsevier.com/locate/jsg

Late Holocene episodic displacement on fault scarps related to interstratal dissolution of evaporites (Teruel Neogene Graben, NE Spain)

F. Gutiérrez [a,*], D. Carbonel [a], J. Guerrero [b], J.P. McCalpin [c], R. Linares [d], C. Roqué [e], M. Zarroca [d]

[a] Departamento de Ciencias de la Tierra, Universidad de Zaragoza, Edificio Geologicas, C/.Pedro Cerbuna 12, Zaragoza, Spain
[b] Department of Geology and Gephysics, Utah State University, USA
[c] Geo-Haz Consulting Inc., Colorado, USA
[d] Departamento de Geología, Universidad Autónoma de Barcelona, Barcelona, Spain
[e] Àrea de Geodinàmica Externa i Geomorfologia, Universitat de Girona, Girona, Spain

ARTICLE INFO

Article history:
Received 28 May 2011
Received in revised form
2 November 2011
Accepted 10 November 2011
Available online 18 November 2011

Keywords:
Nontectonic faults
Monocline
Evaporite collapse
Karstification
Aspect ratio

ABSTRACT

The Mio-Pliocene formations of the Turolian type section (Teruel Graben, Spain) have sagged due to dissolution of the underlying Triassic evaporites generating a 1.7 km long monocline and accompanying synform with 130 m of structural relief. The crest of the monocline is affected by a graben that counterbalances the shortening caused by passive bending in the adjacent syncline. This graben is controlled by a master synthetic fault and a swarm of antithetic and synthetic faults with a conspicuous geomorphic expression. After acquiring Ground Penetrating Radar (GPR) profiles, three trenches were excavated in depressions associated with uphill-facing fault scarps. To our knowledge, these are the first trenches excavated across faults caused by deep-seated dissolution of evaporites. The geometrical relationships observed in two trenches indicate late Holocene episodic displacement (as many as 3 events). Some of the parameters estimated for the investigated faults are clearly different from those expectable for tectonic faults in this intraplate area. They include high apparent vertical slip rates (0.6–1 mm/yr), low average recurrence of faulting events (1.2–2 ka) and very high displacement per event values (>65 cm) for surface ruptures less then 200 m long. Our findings suggest that considering evaporite collapse faults as creeping structures is not a reliable criterion to differentiate between tectonic faults (seismogenic) and dissolution-induced gravitational faults (nonseismogenic).

1. Introduction

Differentiating between tectonic faults and nontectonic faults constitutes a major challenge for seismic hazard assessment with a still poorly developed scientific basis. Active tectonic faults generated by deviatoric regional stress fields have been profusely studied in recent decades. Conversely, investigations on surface ruptures caused by nontectonic processes are very scarce. Gravitational faults may cause surface deformation, but are not capable of producing significant earthquakes; they are nonseismogenic (Hanson et al., 1999). Misinterpreting nontectonic faults as seismogenic tectonic structures (capable faults) may lead to important seismic hazard overestimates with relevant implications. For example, the Hell Creek Fault, British Columbia, Canada, is considered by the provincial utility (BC Hydro) to be the main seismogenic fault that could impact on the Terzaghi Dam (McCleary et al., 1978; Ertec, 1981), whereas the Geological Survey of Canada attributes this controversial fault to nonseismic gravity failure (Clague and Evans, 1994).

One of the main causes of gravitational deformation and faulting is subsurface dissolution of evaporites. These highly soluble formations are or have been present beneath around 25% of the continental surfaces (Kozary et al., 1968; Ford and Williams, 2007), notably in Europe, the Middle East, North America and Australia. Deep-seated dissolution of evaporites by groundwater flows (i.e. interstratal karstification) leads to downward displacement of the overlying rocks and the subsidence of the ground surface. Dissolution-induced subsidence phenomena result in the development of ductile and/or brittle deformation structures that do not affect the infra-evaporitic formations. Widespread interstratal karstification causes a diminution in the volume of the evaporite formations until they are reduced to a karstic residue, involving a condensation of the stratigraphic sequence. These insoluble residues are typically associated with collapse breccias resulting

* Corresponding author. Tel.: +34 976 761090; fax: +34 976 761106.
E-mail address: fgutier@unizar.es (F. Gutiérrez).

0191-8141/$ – see front matter © 2011 Elsevier Ltd. All rights reserved.
doi:10.1016/j.jsg.2011.11.006

from the fracturing of the less soluble sediments situated within and above the karstified units (e.g. Stanton, 1966; James and Choquette, 1987; Sasowsky et al., 2008). Collapse breccias may cover extensive areas and some of them may constitute highly prolific reservoirs for water and hydrocarbons (e.g. the heavy-oil reservoir of the Upper Devonian Grosmont Formation in Alberta, Canada; Cutler, 1983) or may host valuable mineralizations (Warren, 1997; 2006). According to Warren (2006), there are more evaporite dissolution-induced collapse breccias and karstic residues in the stratigraphic record than there are evaporitic formations, since these rocks have been removed to a great extent by subsurface dissolution.

Interstratal dissolution of evaporites may generate a wide variety of deformation structures (Warren, 2006; Gutiérrez and Cooper, in press), including active faults with a surface expression. The cartographic scale of these structures may be of the order of hundreds of kilometres and strain rates may reach values significantly higher than those reported for tectonic structures due to the high solubility of the evaporites. The equilibrium solubilities of gypsum and halite, the most common evaporitic minerals, are 2.4 gr/l and 360 gr/l, respectively. Widespread interstratal evaporite dissolution generally causes sagging in the overlying strata and the development of structural basins with centripetal dips. The resulting depressions may act as depositional basins in which sediments accumulate recording dissolution-induced synsedimentary subsidence phenomena. Evaporite units beneath these basins wedge out towards the center of the structure, whereas the strata of the basin fill show cumulative wedge outs with progressive basinward thickenings and upward dip attenuation. In the Delaware Basin, New Mexico and Texas, dissolution of Permian evaporites has generated depositional basins more than 150 km long filled with Neogene continental sediments that reach around 500 m in thickness (Maley and Huffington, 1953; Olive, 1957; Baumgardner et al., 1982; Bachman, 1984; Hill, 1996). Kirkham et al. (2002), in the Carbondale collapse center, Rocky Mountains of Colorado, documents subsidence basins generated by subjacent evaporite dissolution filled with alluvium up to 450 m thick.

Interstratal karstification of evaporites frequently migrates laterally in a downdip direction producing monoclinal flexures in the supra-evaporitic units atop the dissolution fronts (Warren, 1997; Gutiérrez and Cooper, in press). These drape folds of gravitational origin may constitute good traps for hydrocarbons (Anderson et al., 1988; Anderson and Knapp, 1993; Warren, 2006). The retreating front of the monoclines may be expressed at the surface by updip-facing scarps. The subsidence depressions associated with these monoclines may act as depositional basins and control the development of lakes as well as the position and migration of fluvial systems (e.g. Walters, 1978; Anderson et al., 1994; Anderson and Hinds, 1997). This type of structure has been documented in a number of regions including northern England (Cooper, 2002), Canada (Hopkins, 1987; Anderson et al., 1988), the Paleozoic evaporite basins of the southwest and central sectors of the USA (De Mille et al., 1964; Walters, 1978; Anderson et al., 1994; Neal and Colpitts, 1997; Kirkham et al., 2002) or NE Thailand (Supajanya and Friederich, 1992). Probably, the most dramatic example is the more than 550 km long monoclinal fold and scarp developed in the Interior Homocline of Central Saudi Arabia. Here, the downdip migration of dissolution fronts in the east-dipping anhydrite units of the Late Jurassic Hit and Arab formations has caused the subsidence of the overlying sequence, producing a west-facing sinuous monoclinal escarpment (Powers et al., 1966; Memesh et al., 2008). This monocline is affected by numerous caprock collapse sinkholes as well as crestal normal faults and fissures with conspicuous geomorphic expressions. Subsidence due to interstratal dissolution of evaporites may also play a significant role in the evolution of major fluvial systems. According to Gustavson (1986), the development of the Canadian River valley in the Texas Panhandle, for 200 km of its length, is largely related to subsidence due to the downward and lateral migration of dissolution fronts in deep-seated salt units, rather than to erosional lowering.

Differential interstratal dissolution of evaporites may also result in the formation of faults passing through the supra-evaporitic units and the development of grabens, foundered blocks controlled by circular or ellipsoidal faults and collapse structures bounded by failure planes with highly irregular cartographic traces. In the Paradox fold and fault belt of Utah and Colorado, subsidence of the crests of anticlines cored by halokinetic salt walls, up to 4 km thick, has resulted in the development of a series of grabens up to 50 km long. These depressions are controlled by active gravitational normal faults with vertical throws in excess of 1 km (Cater, 1970; Doelling, 2000; Gutiérrez, 2004). In northern Michigan, Black (1997) reports karst graben valleys around 0.5 km wide generated by interstratal dissolution of Middle Devonian gypsum controlled by pre-existing tectonic faults and joints. The Needles Fault Zone, Utah, is an arcuate system of grabens (Grabens of Canyonlands) covering about 200 km^2. These extensional structures have been developed at the margin of the 360–530 m deep Cataract Canyon dissected by the Colorado River. Here, the exposed stratigraphic sequence has a general dip towards the canyon and is composed of a sequence of competent limestones and sandstones 460 m in thickness, lying on the salt-bearing Paradox Formation. The development of these active grabens, up to 6 km long and 100 m deep have two causes. They are related to extension in the upper rigid plate caused by the downdip lateral flow of the Paradox Formation towards the canyon (lateral spreading due to salt flowage), that formed the Meandering Anticline. They are also caused by subsidence due to dissolution of the evaporites, as shown by the presence of saline springs in the river (McGill and Stormquist, 1979; Huntoon, 1982; Moore and Schultz, 1999; Baars, 2000; Trudgill, 2002). In the Calatayud Neogene graben, NE Spain, Gutiérrez (1996) documents two collapse areas with highly tortuous boundaries covering 8 and 14 km^2. In these structures, the supra-evaporitic Miocene sequence, around 100 m thick, has undergone intense deformation and vertical displacement in excess of 200 m due to the interstratal karstification of the underlying halite- and glauberite-bearing Tertiary formation. The 45 km long structural basin of the Saskatoon Low, Saskatchewan, Canada, is controlled by gravity faults and has a structural relief equal to the thickness of the Devonian salt unit that has been partially removed by dissolution (180 m) (Christiansen, 1967; Christiansen and Sauer, 2001). In the Rocky Mountains of Colorado, Kirkham et al. (2002) illustrates an example of flexural slip faulting and the formation of uphill-facing scarps caused the unfolding of steeply dipping strata due to dissolution of the underlying salt-bearing evaporites.

According to Huntoon (1999), dissolution-induced faults may have similar structural and geomorphic appearance as tectonic faults, and consequently the key for elucidating their origin is to properly understand their boarder geologic context. Some of the criteria that may be used to identify nontectonic faults related to interstratal dissolution of evaporites include: (1) Extent and thickness of evaporite formations in the area. The distribution of faults related to evaporite dissolution is restricted to the areas occupied by these formations at the present time or in the past. Moreover, cumulative vertical displacement in the collapse structures cannot exceed the original thickness of the evaporites. (2) Geometry of the faults in plan view. Evaporite dissolution-induced faults may have circular, ellipsoidal or highly sinuous cartographic geometries (Christiansen, 1971; Gutiérrez, 1996). (3) Vertical extent of the faults. Evaporite collapse faults do not affect the infra-

evaporitic rocks. (4) Analysis of the trend and styles of the deformation structures in an area, which may help to identify faults exclusively related to evaporite karstification. The strike-slip displacement component on gravitational faults resulting from dissolution-induced subsidence is negligible. (5) Construction of isopach maps and geological cross-sections, which may indicate a clear spatial correspondence between the dissolution-induced thinning of evaporite formations and the topographic depressions plus the distribution and thickening of younger units; sediments filling dissolution-induced basins. (6) Presence of geomorphic and hydrological features indicative of subsurface evaporite dissolution; sinkholes, subsidence basins, hummocky topography, subsurface drainage, swallow holes, saline springs (Gutiérrez and Cooper, in press). (7) The aspect ratio of faults. Dissolution-induced fault scarps are generally higher than those associated with tectonic faults of the same length (Hanson et al., 1999). (8) The slip rates, typically significantly higher than those of seismogenic tectonic faults. (9) Microseismic surveys, which may indicate shallow gravitational faulting caused by loss of basal support as a result of evaporite dissolution.

In this work we investigate in Teruel Neogene Graben, NE Spain, a syncline and a monocline affecting the sediments proposed for the Turolian stratotype and generated by interstratal dissolution of Triassic evaporites. The crest of the monocline is affected by a graben with conspicuous geomorphic expression. To our knowledge, this is the first time that fault scarps related to evaporite dissolution have been investigated by means of the trenching technique. The main aims of the work include: (1) Characterise the gravitational structures from the structural and geomorphological point of view. (2) Obtaining data on the age of the surface gravitational faults. (3) Analyse the kinematics of the faults elucidating whether they have a progressive or continuous displacement regime. (4) Characterise the activity of the faults estimating parameters like the slip rate, displacement per event or recurrence of faulting events. (5) Explore criteria that might help to differentiate between tectonic and non-tectonic structures caused by evaporite dissolution.

2. Geological and geomorphological setting

The study area is located 2 km NE of Teruel city in the central sector of Teruel Neogene Graben, a post-orogenic basin developed within the Iberian Chain, NE Spain (Fig. 1). The Iberian Chain is an intraplate Alpine orogene with a prevailing NW-SE structural grain generated by the tectonic inversion of Mesozoic extensional basins from late Cretaceous to Early-Middle Miocene times. During the post-orogenic stage, several grabens superimposed on the previous compressional structures were created in two main rifting phases (Capote et al., 2002; Gutiérrez et al., 2008a). The formation of the NNE-SSW oriented Teruel Neogene Graben, located in the south-eastern sector of the Iberian Chain, started during the first extensional phase in the Middle Miocene (Alcalá et al., 2000) (Fig. 1). The genesis of this ca. 100 km long and up to 20 km wide extensional structure is attributed to the westward propagation of the rifting process that developed the offshore NE-SW trending Valencia Trough (Anadón and Moissenet, 1996; Anadón and Roca, 1996; Capote et al., 2002). The Late Pliocene-Quaternary Jiloca Depression formed in the second extensional phase (Simón, 1989; Gracia et al., 2003; Capote et al., 2002). The southern portion of this asymmetric basin, controlled by the 24 km long Concud-Teruel Fault on its eastern margin, is superimposed on the west-central sector of Teruel Graben (Fig. 1). The Concud-Teruel Fault, with a general NW–SE strike in its northern sector, turns into a N–S

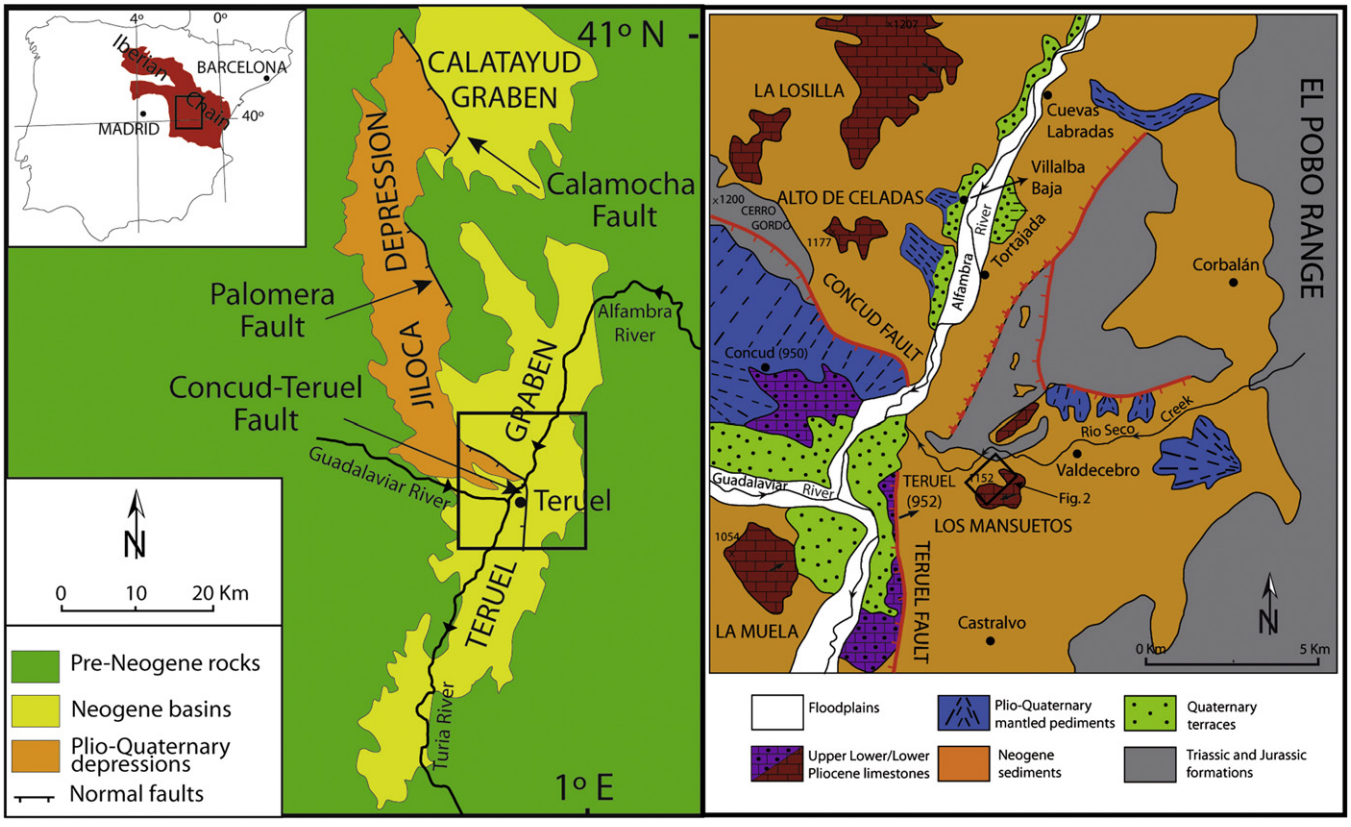

Fig. 1. Geological setting of the study area in the Iberian Chain and the in the post-orogenic Teruel Neogene Graben. Inset in the right figure indicates the approximate area mapped and shown in Fig. 2.

direction in the western margin of the Alfambra River valley, cropping out further south at the opposite side of the valley with a N–S trend, where it is named Teruel Fault (Gutiérrez et al., 2008a).

The Middle Miocene-Upper Pliocene sedimentary fill of Teruel Graben, more than 300 m thick and deposited under endorheic conditions, is composed of alluvial fan deposits that grade towards the depocentral sectors of the basin into carbonate and gypsum lacustrine facies (Hernández and Anadón, 1985; Alcalá et al., 2000; Alonso-Zarza and Calvo, 2000). In the Early Pliocene, lake environments reached a great extent in the central sector of the basin, with the deposition of extensive limestone units that form the caprock of several mesas situated in the surroundings of Teruel city (Los Mansuetos, La Muela, Alto de Celadas, La Losilla; Mein et al., 1989-1990; Alonso-Zarza and Calvo, 2000) (Fig. 1). In the Late Pliocene, deposition was restricted to a residual carbonate lake situated in the hanging wall of the Concud-Teruel Fault (Moissenet, 1983; Mein et al., 1989-1990). In the footwall of the Concud Fault, the top of the Lower Pliocene limestone unit capping the Alto de Celadas and La Losilla mesas matches attitudinally with a planation surface cut-across folded Mesozoic formations at Cerro Gordo (~1200 m) (Fig. 1). This Lower Pliocene morpho-stratigraphic marker, with a maximum age of 3.6 Ma, has been offset vertically by around 250 m on Concud-Teruel Fault, yielding a minimum long-term vertical slip rate of 0.07 mm/yr (Gutiérrez et al., 2008a).

The Teruel Basin, which is essentially a half-graben controlled by master normal faults on the eastern margin, is drained longitudinally by the deeply entrenched Turia and Alfambra rivers, the latter transversally crossing Concud Fault (Fig. 1). This endorheic basin was captured by the Turia River through its southern edge, most probably in Early Pliocene times (Adrover et al., 1978; Gutiérrez et al., 2008a). The new exorheic and incisional drainage expanded progressively towards the northern sector of the basin. The change from endorheic to exorheic conditions in the central sector of Teruel Graben is recorded by Upper Pliocene alluvial fan sediments unconformably overlying Upper Pliocene limestones (Mein et al., 1989-1990). This alluvial fan unit, deposited after an erosional phase, is inset in the endorheic basin fill and capped by mantled pediments inclined towards the current drainage (Gutiérrez, 1998; Gutiérrez et al., 2008a) (Fig. 1). The shift to exorheic conditions constitutes a crucial landmark in the hydrogeological evolution of a sedimentary basin and has an instrumental influence on the development of dissolution-induced gravitational deformation. Under an endorheic regime, the solutes transported by groundwater flows are ultimately accumulated as chemical deposits in terminal discharge lakes (Rosen, submitted for publication; Yechieli and Wood, 2002). Once the basins are captured and dissected by an exorheic drainage network, groundwater flows enhanced by higher hydraulic gradients may dissolve large quantities of evaporites that are ultimately evacuated by fluvial systems (Gutiérrez, 1998).

The Neogene sediments of Teruel Gaben fill show a dominant subhorizontal structure locally affected normal faults with decametre- to hectometre-scale throws (i.e. Concud-Teruel Fault). Conversely, in the areas where the Neogene sediments overlie Triassic evaporitic bedrock, gravitational structures caused by subsidence due to interstratal karstification are abundant. In the intrabasinal inlier of folded Mesozoic formations located North of Los Mansuetos, Gutiérrez (1998) documents outcrops of Neogene detrital and carbonate sediments that show evidence of gravitational deformation restricted to the sectors where the bedrock corresponds to Triassic evaporites (Fig. 1): (1) Hectometre-scale basin structures with centripetal dips and cumulative wedge outs affecting alluvial fan deposits that grade into carbonate palustrine-lacustrine facies towards the core of the basins. These structures record local dissolution-induced synsedimentary subsidence phenomena that led to the formation of sagging sinkholes with small carbonate-producing lakes in alluvial fan environments. Gutiérrez (1998) proposes that these features may constitute the stratigraphic evidence for the karstification process involved in the recycling of evaporites during the Neogene, whereby dissolved Triassic evaporites were reprecipitated as gypsum formations in the Teruel Graben (Utrilla et al., 1992). (2) Warped and folded sediments showing rapid discordant changes in strike and dip, locally reaching 80°. These structures are attributed to spatially variable passive bending related to differential subjacent dissolution. (3) Transtratal collapse breccias with well-defined boundaries resulting from upward stoping of cavities and the development of breccia pipes.

This investigation is focused on the gravitational structures developed on the NW flank of Los Mansuetos mesa and along the Rio Seco Creek, where dissolution of Triassic evaporites has caused the downward flexure of the overlying Mio-Pliocene formations (Fig. 2). The subsidence phenomenon has produced a synform and a monocline, the crest of which is affected by a keystone graben 1.7 km long with conspicuous geomorphic expression (Figs. 3 and 4). An additional interest of these peculiar structures is that they affect the fossil-rich sections proposed for the stratotype of the Turolian, a Mediterranean Neogene continental stage (Crusafont, 1965; Marks, 1971; Aguirre, 1975; Aguirre et al., 1975; Mein, 1990; Calvo et al., 1999). As Calvo et al. (1999) state, improving the geological background of this complex structural area would benefit the formal definition of the Turolian type section.

3. Methodology

The investigation followed a phased approach. Initially, a detailed 1:5000 scale geological map of the study area was produced including information on the stratigraphy, structure, geomorphology and Quaternary deposits (Fig. 2). Special attention was paid on the distribution of fault scarps and the associated recent graben deposits as targets for the trenching investigation. This cartography was essentially carried out by direct mapping in the field on 1:5000 scale colour orthophotographs. Aerial photographs of 1:20,000 approximate scale helped to refine the delineation of some cartographic elements. The geological map of Los Mansuetos produced by Calvo et al. (1999) was a highly useful reference. The map was digitized using AutoCAD 2008 on a georeferenced 1:5000 topographic map with a contour interval of 5 m. The geological cross-sections were also constructed with AutoCAD 2008 in order to facilitate structural measurements (Fig. 5). The height of the fault scarps were measured in the field using a laser hypsometer (Laser Atlanta, Advantage).

In a subsequent phase, 4 sediment-filled troughs associated with uphill-facing fault scarps were selected as potential trenching sites. A total of 12 Ground Penetrating Radar (GPR) profiles ranging from 10 to 50 m in length were acquired in these morpho-structures, all them oriented transverse to the linear depressions. The aim of these geophysical surveys was to obtain information on the position of failure planes and the approximate thickness and extent of the trough fills. This indirect and non intrusive method helped us to select the *a priori* most favourable sites for the excavation of trenches. The profiles were acquired with an IDS (Ingegneria Dei Sistemi S.p.A.) GPR equipped with a 100 MHz antenna and using the IDS software K2FastWave with the default configuration: (1) Range of 256 ns with 100 MHz frequency and 512 samples per scan. (2) A propagation speed of 10 cm/ns (3) A wheel pace (step) and resolution of 0.048 m. The processing of the radargrams was carried out with the IDS software GRED applying the filters: move start time, background removal, vertical bandpass and linear gain.

Three trenches 13–16 m long and up to 2.5 m deep were excavated with a tracked hydraulic excavator in the depressions associated with three different antislope fault scarps (see location

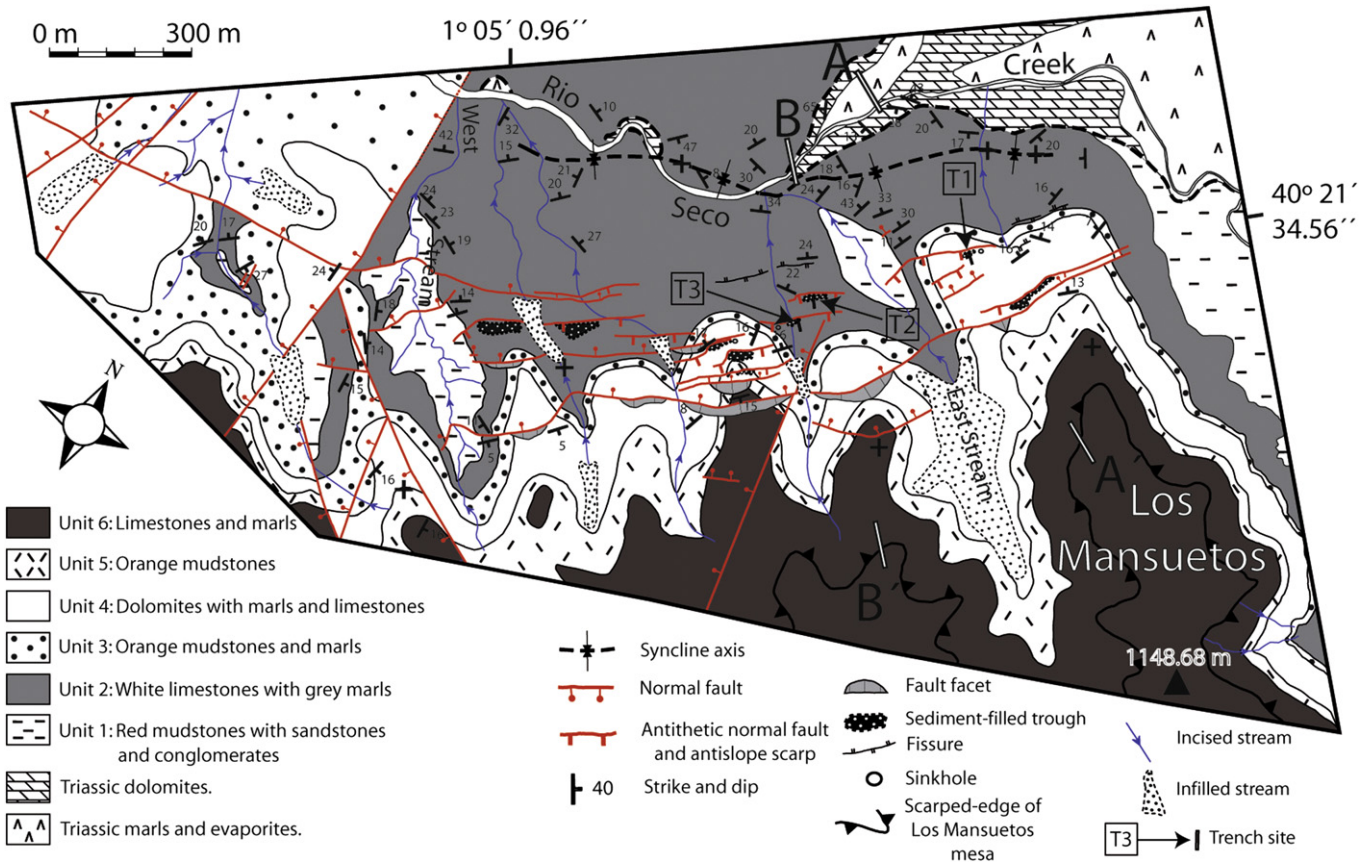

Fig. 2. Geological map of the NW flank of Los Mansuetos mesa, where the Neogene sequence has subsided due to interstratal dissolution of Triassic evaporites forming a monocline with a crestal graben and a sinuous syncline of the lower flexure.

in Fig. 2). All trenches were oriented perpendicularly to the strike of the investigated structures. We followed the classical procedure applied for the study of paleoseismological trenches (McCalpin, 2009a). After cleaning the trench walls, a reference grid with horizontal and vertical strings spaced 0.5 or 1 m apart was placed on the shaded side of the trench, which was logged on graph paper at a scale of 1:50. Material datable by the radiocarbon method (snails, charcoal and wood) was collected in the excavated deposits,

Fig. 3. General view of the NE sector of the Rio Seco gravitational syncline and monocline, the latter affected by a crestal graben (indicated by arrows). The image, looking to the NE, shows the periclinal termination of the synform.

Fig. 4. Northeastern sector of the keystone graben developed in the crest of the Rio Seco monocline. The main synthetic and antithetic faults of this keystone crestal graben control conspicuous downhill- and uphill-facing scarps, respectively. Note the drag fold in the hanging wall of the main antithetic fault.

preferably in the units situated at the base of the graben fill and in those located just beneath and above the stratigraphic discontinuities recording faulting events (event horizons). The obtained AMS radiocarbon ages were calibrated using CALIB 6.0.1 and the data set intcal 09.14c of Reimer et al. (2009) (Table 1).

4. The gravitational structures and associated landforms

4.1. Stratigraphy

The oldest rocks that crop out in the mapped area correspond to the Middle Triassic Muschelkalk lithofacies. In this sector of the Iberian Chain the Muschelkalk is composed of two dolomitic units (M1 and M3) separated by an intermediate unit made up of marls, mudstones and evaporites (M2). In the Rio Seco Creek we have identified outcrops of the M2 and M3 units (Fig. 2), which record a regression–transgression cycle of the Tethys Sea in the Iberian Basin; the Ladinian depositional sequence (Riba, 1991; Meléndez et al., 1995). In outcrop, the M2 evaporitic unit, which is responsible for the analysed gravitational deformation structures, displays multicoloured marls and clays with secondary gypsum beds. Boreholes drilled in the eastern sector of the Iberian Chain indicate that this unit, deposited in a transitional environment with extensive hypersaline lagoons and sabkhas, may include halite deposits up to 300 m thick in the subsurface (Ortí et al., 1996). Unfortunately, no borehole data are available from the vicinity of the area. Most likely the exposed M2 sediments correspond to a condensed sequence resulting from the removal of the most soluble halite facies by subsurface dissolution, as is commonly the case in many salt-bearing evaporitic formations (i.e. Warren, 2006; Gutiérrez and Cooper, in press).

The Upper Miocene-Lower Pliocene succession unconformably overlies the folded Mesozoic rocks (Fig. 2). It shows a significant thickness increase towards the south, away from the intrabasinal inlier of Mesozoic formations N of the Rio Seco Creek, which acted as a topographic high during the infill of the basin (Fig. 1). In the Rio Seco valley we have estimated an original thickness of around 90–100 m for the Neogene cover, whereas in the SE flank of Los Mansuetos mesa it has a minimum outcropping thickness of 200 m. In our map we have followed the six lithostratigraphic units differentiated by Calvo et al. (1999) in their geological study of Los Mansuetos. From base to top these are (Fig. 2):

Unit 1 (Upper Vallesian): Red mudstones with intercalated sandstone and conglomerate beds. The variations in thickness of this unit accounts for most of the southward thickening of the Neogene sequence. An outcropping thickness of 25–30 m has been measured in the gullies dissecting the SE slopes of the Rio Seco valley.

Unit 2 (Upper Vallesian): 10–15 m of white biomicritic and tufaceous limestones with intercalations of grey marls. This is one of the units with a large cartographic expression, since it forms the dip slope of the NW flank of Los Mansuetos.

Unit 3 (Lower Turolian): 7–10 m of reddish orange mudstones and marls with sandstone beds.

Unit 4 (Lower-Upper Turolian): around 10 m of dolomites with marl and limestone beds.

Unit 5 (Upper Turolian): 5–10 m of orange mudstones with some gypsum.

Unit 6 (Lower Pliocene): 25–30 m of alternating limestones and marls. The top of this unit forms the structural surface of Los Mansuetos mesa.

4.2. Structure and geomorphology

Los Mansuetos mesa is located in the footwall of the N–S trending and W dipping Teruel Fault (Fig. 1). That is, it forms part of the Teruel Neogene Graben fill and is located in the eastern margin of the Jiloca Plio-Quaternary fault-angle depression. The Neogene sequence lies on an angular unconformity that truncates folds affecting Middle Triassic evaporites and dolomites (M2 and M3). These alpine folds veer from an NNE-SSW to an NE-SW trend just north of Los Mansuetos mesa. Two sets of tectonic normal faults

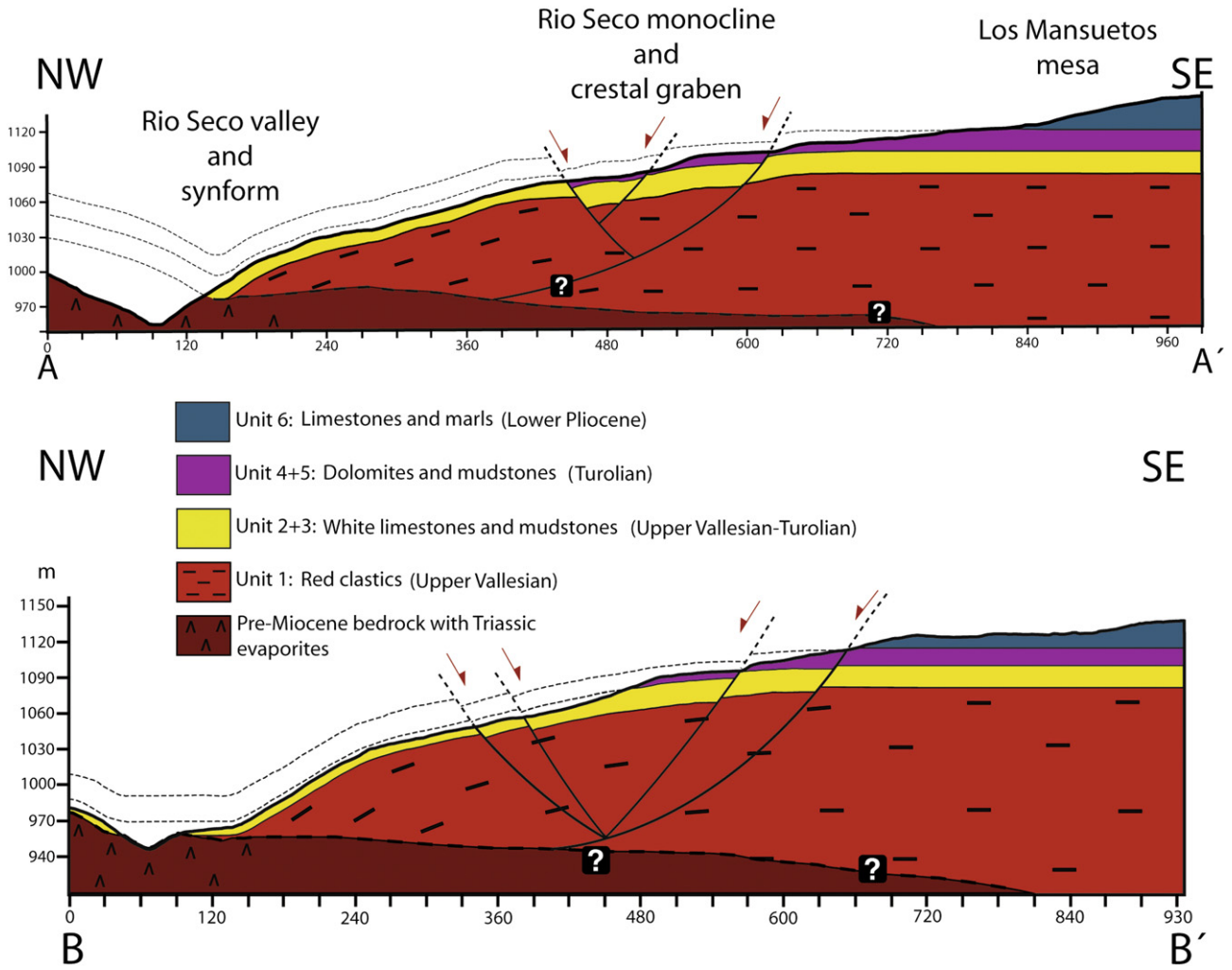

Fig. 5. Cross-sections displaying the geometry of the gravitational structures related to subjacent dissolution of Triassic evaporites in the Rio Seco valley and the NW flank of Los Mansuetos mesa. The trace of the sections is indicated in Fig. 2.

have been identified in the mapped area (Fig. 2): (1) N–S to NNW-SSE, down to the west faults situated in the western sector of Los Mansuetos. These structures, with vertical offsets of 10–15 m, appear to be linked to the nearby N–S oriented Teruel Fault. Their development is probably related to the formation of the Jiloca Half-graben, which started in the Late Pliocene. (2) Two NW–SE faults with 5–10 m in vertical separation. The available geometrical relationships do not allow us to establish a relative chronology for these two fault sets.

In the NW flank of Los Mansuetos mesa, passive bending of the Neogene formations due to interstratal karstification of the underlying Triassic evaporites has produced an NE-SW trending and 1.7 km long monocline with a synform in the lower flexure (Figs. 3 and 5). Dissolution-induced gravitational deformation has also affected the Triassic dolomites where the Neogene sequence rests on these carbonate rocks. In these sectors the Triassic dolomites are intensely brecciated and show highly variable strikes and dips where the stratification is recognisable. The Río Seco valley follows the syncline concordantly and its SE margin corresponds to the dip slope that forms the NW-facing monoclinal scarp. Several streams incised into this dip slope allow examination of the gravitational flexure and faults affecting the Miocene strata. The dip of units 1 to 5 increases sharply in the crest of the monocline and units 1 and 2 dip up to 40° towards the valley in the monoclinal scarp (Fig. 2). The structural relief of the monocline reaches 130 m (Fig. 5). This figure provides a measure of the cumulative subsidence magnitude and the minimum thickness of evaporites removed by subsurface dissolution. The monoclinal flexure attenuates towards the NE and its northeastern termination has been truncated by erosion. The SW termination of the monocline coincides with the N–S trending normal fault situated to the west of the West Stream (Fig. 2). The axis of the lower synform, whose location has been identified in several reaches of the Rio Seco valley, shows a sinuous trace. This syncline attenuates sharply in the NE sector of the structure forming a tight pericline (Figs. 2 and 3). Locally, strata dipping to the SE have been identified in the Rio Seco valley, however, the NW limb of the syncline has been largely removed by erosion.

The crest of the monocline is affected by a keystone graben 1.7 km long with a conspicuous geomorphic expression, indicating recent activity (Fig. 4). This extensional structure counterbalances the shortening of the Neogene cover caused by sagging in the adjacent syncline (Fig. 5). The graben is controlled by a master synthetic fault and a swarm of secondary antithetic and synthetic faults with en echelon distribution. The width of the graben (140–300 m) and the number of faults (2–6) decreases towards the NE edge, consistently with the attenuation of the monoclinal and synclinal flexures (Fig. 2). In the SW sector of the graben there is a 1.3 km long synthetic normal fault with around 8 m in vertical

Table 1
Code of sample dated by AMS, trench, laboratory number (Poz: Poznan Radiocarbon, Beta: Beta Analytic), material, conventional radiocarbon ages, calibrated dates at 2 sigma (using CALIB 6.0.1 and the data set intcal 09.14c; Reimer et al., 2009). In bold calibrated age ranges with relative area higher than 0.1.

Code and trench	Lab. number	Material	Conventional C-14 age	Calibrated age (2 σ)	Calibrated age (2 σ)
Te-19	Beta - 294639	Terrestrial snail	3270 ± 30 BP	**1622–1492 BC (0,960625)**	**3572–3442 BP (0,960625)**
Trench 1				1478–1458 BC (0,039375)	3428–3408 BP (0,039375)
Te-17 Trench 1	Beta - 294638	Charcoal	90 ± 30 BP	1685–1732 AD (0,271703)	**265–218 BP (0,271703)**
				1808–1928 AD (0,715317)	**142–22 BP (0,715317)**
				1951–1954 AD (0,01298)	1951–1954 AD (0,01298)
Teruel 12 Trench 2	Beta - 294636	Wood	3020 ± 30 BP	**1389–1192 BC (0,974839)**	**3339–3142 BP (0,974839)**
				1174–1167 BC (0,008499)	3124–3117 BP (0,008499)
				1142–1133 BC (0,016662)	3092–3083 BP (0,016662)
Te-15A Trench 3	Beta - 294637	Terrestrial snail	2350 ± 40 BP	727–693 BC (0,033393)	2677–2643 BP (0,033393)
				657–655 BC (0,001357)	2607–2605 BP (0,001357)
				542–361 BC (0,959301)	**2492–2311 BP (0,959301)**
				271–262 BC (0,00595)	2221–2212 BP (0,00595)
Te-16 Trench 3	Poz - 38878	Charcoal	1920 ± 35 BP	**1–143 AD (0,954109)**	**1949–1807 BP (0,954109)**
				146–173 AD (0,027137)	1804–1777 BP (0,027137)
				193–210 AD (0,018753)	1757–1740 BP (0,018753)
Te-5 Trench 3	Poz - 38879	Terrestrial snail	1850 ± 30 BP	**85–235 AD (1)**	**1865–1715 BP (1)**
Teruel 7 Trench 3	Beta - 294635	Charcoal	170 ± 30 BP	**1660–1698 AD (0,183566)**	**290–252 BP (0,183566)**
				1722–1817 AD (0,535192)	**228–133 BP (0,535192)**
				1833–1879 AD (0,08345)	117–71 BP (0,08345)
				1916–1953 AD (0,197792)	**34–0 BP (0,197792)**
Teruel 6 Trench 3	Beta - 294634	Charcoal	30 ± 30 BP	**1695–1726 AD (0,197719)**	**255–224 BP (0,197719)**
				1813–1838 AD (0,139833)	**137–112 BP (0,139833)**
				1842–1853 AD (0,023844)	108–97 BP (0,023844)
				1868–1873 AD(0,007839)	82–77 BP (0,007839)
				1876–1918 AD (0,602316)	**74–32 BP (0,602316)**
				1952–1954 AD (0,028451)	0 BP (0,028451)

separation that crosses the N–S tectonic faults located west of the West Stream, clearly displacing one of them; the gravitational fault postdates the tectonic faults. The 1.5 km long master synthetic fault crops out in the West Stream, where we have measured a vertical separation of 5.5 m and a 50 NW dip (Fig. 6A). Here, an exposure of the fault plane shows striations indicative of dip-slip displacement. The vertical offset measured on our map in the central sector of this fault is around 9 m. This master fault controls a prominent downslope-facing scarp with broad facets up to 12 m high (Fig. 6B). The height of the facet, higher than the vertical offset, may be explained by faulting on a steep or scarped slope and subsequent erosional broadening of the facet.

The antithetic faults, 80–345 m long, are considerable shorter than the secondary synthetic faults. The East Stream has a good exposure of the deformation caused by an antithetic fault on the Miocene units 1 and 2 (Fig. 6C). Here, a clearly distinguishable limestone layer is offset vertically 9 m on the fault, dipping 45–50° into the slope, and shows an obvious drag fold in the hanging wall. In the central sector of the graben the trace of two antithetic faults show a sharp bend (Fig. 2). This geometry may be related to the linkage of two en echelon faults through the failure of an accommodation ramp in the step over zone. This involves the transformation of a two soft-linked faults into two hard-linked fault segments (McGill and Stormquist, 1979; Walsh and Watterson, 1988; Cartwright et al., 1995; Trudgill, 2002). The antithetic faults have created 7 sackung-like uphill-facing scarps on limestone, reaching 345 m in length and 3 m height (Fig. 2). Linear troughs acting as sediment traps have been formed on the upslope side of these fresh-looking antislope scarps (Fig. 6D). Locally the upslope-facing scarps control deflections in the drainage and have caused temporary obstructions in streams creating closed depressions (site of Trench 3). There is also some correlation between the distribution of the antislope scarps and that of the incised and infill reaches of the transverse streams, the latter being more frequent upstream of the scarps (Fig. 2). Extension in the graben area has also produced ground fissures up to 226 m long and 5 m wide, some of which form prominent trenches open in competent limestone beds of unit 2 (Fig. 6D). Cover collapse sinkholes up to 3 m in diameter are also relatively common (Fig. 6F). They mainly occur on the deposits filling the sackung troughs. Their formation is attributed to the downward migration (ravelling) of cover deposits through concealed open fissures in the bedrock. Sinkholes associated with gravitational sackung features have been previously reported by McCalpin and Irvine, (1995) and Gutiérrez et al. (2008b).

The maximum height of the uphill-facing and downhill-facing fault scarps has been measured in the field avoiding areas with evidence of erosion at the foot (Table 2). Fig. 7 presents a plot of scarp length (L), measured as a straight line, versus scarp height (H_{max}). Uphill- and down-facing scarps show a general direct relationship, with higher heights for increasing length. The average aspect ratio (H_{max}/L) of the 8 uphill-facing scarps is 0.0081, ranging from 0.004 to 0.017 and with a standard deviation of 0.0047. This population data shows a low coefficient of determination for a power law regression ($H_{max} = 3.2929\ L^{0.5202}$, $R^2 = 0.269$). The 5 downhill-facing scarps have an average aspect ratio (0.029) one order of magnitude higher and a much better goodness of fit ($H_{max} = 9.4177\ L^{0.5842}$, $R^2 = 0.829$).

Using cross-sections A-A′ and B-B′ and considering the flexure situated SE of the syncline axis, we have calculated that gravitational sagging involves a shortening of 16 m (5%) and 19 m (6.8%), respectively (length of the strata vs. horizontal distance between the synform axis and NW boundary of the crestal graben; Fig. 5). Horizontal extension (E) produced by each fault on cross-sections A-A′ and B-B′ has been estimated using the dip (β) and vertical displacement of the faults (H), both measured in the field or estimated from the map ($E = H/\tan\beta$). Estimated cumulative extension due to dip-slip displacement on the mapped faults on cross-sections A-A′ and B-B′ is 12 m and 9 m, respectively. These low extension values compared to those estimated for shortening in both cross-sections, are most likely related to the fact that the actual number of normal faults that accommodate extension is higher that that depicted in the map, as indicated by the concealed structure exposed in the trenches. Additionally the cross-sections do not include the stretching caused by horizontal separation (dilation) on faults and fissures.

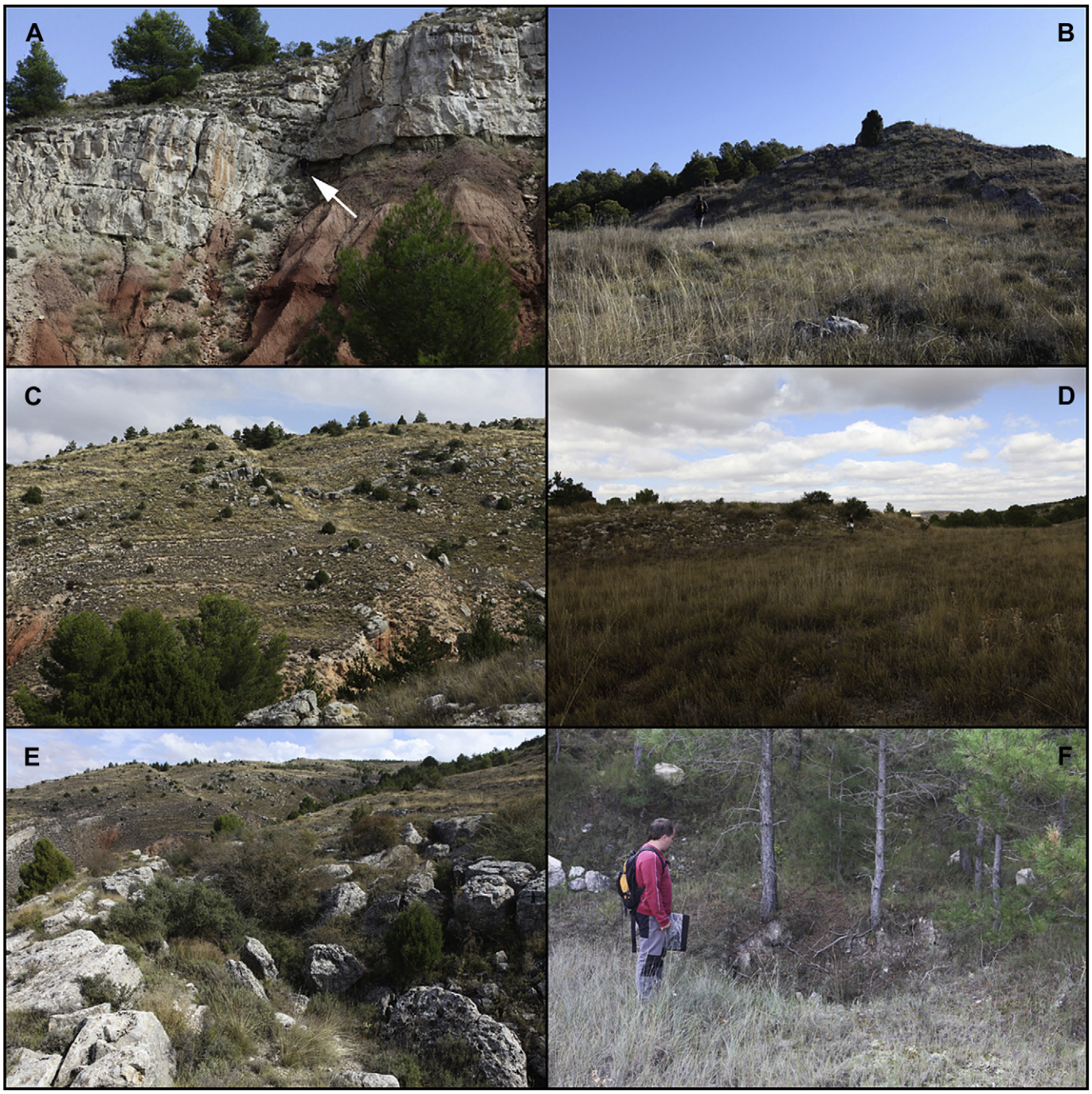

Fig. 6. A: Outcrop at the West Stream of the master synthetic fault of the keystone graben developed in the crest of the monocline. Here, the exposed fault plane shows striations indicative of dip-slip displacement. Arrow points to a person for scale. B: Facet on downhill-facing scarp associated with the synthetic master fault of the crestal graben. C: Antislope scarp controlled by an antithetic fault in the East Stream. Note the drag fold in the hanging wall. D: Linear depression filled of recent deposits at the foot of a sackung-like uphill-facing scarp. E: Ground fissure on limestone on the dip slope located west of the East Stream. F: Collapse sinkhole related to the downward migration of cover material through underlying extensional fissures.

5. Trenching

5.1. Selection of trench sites

Locations of the trenches excavated in the fault-controlled depressions were based on the following criteria: (1) Accessibility. Some favourable sites were discarded because they were not accessible even with a trackhoe. (2) Structural diversity. The trenches were excavated in depressions controlled by three different antithetic faults. (3) Geomorphic diversity. Trenches 1 and 2 were dug in linear depressions developed in slopes with steep overall gradients. Trench 3 was sited in a depression formed in a drainage upstream of an antislope fault scarp (Fig. 2). (4) Sites where the trough fill does not show any surface evidence of erosion were selected, in order to obtain a more complete and continuous record. (5) Not disturbing trees was mandatory.

Table 2
Maximum height, length and aspect ratio of mapped fault scarps in the graben developed at the crest of the Rio Seco monocline. The antislope scarps across which the trenches have been excavated are indicated.

	Height (m)	Length (m)	Height/Length
Uphill-facing scarps			
2	1.47	345.27	0.0042
4	0.64	80.35	0.0079
5 (Trench 1)	3.45	254.41	0.0135
6	0.99	252.12	0.0039
7	2.41	136.16	0.0176
8 (Trench 3)	1.41	177.89	0.0079
9 (Trench 2)	1.01	121.12	0.0083
11	2.39	461.75	0.0051
14	0.95	225.02	0.0042
Average	1.63	228.23	0.0080
Standard deviation	0.92	119.29	0.0047
Downhill-facing scarps			
1	12.52	1531.15	0.0081
3	8.4	102.58	0.0818
10	4.3	583.95	0.0073
12	10.5	222.04	0.0472
13	3.09	1323.47	0.0023
Average	8.98	752.64	0.0293
Standard deviation	5.15	645.07	0.0344

5.2. Trench 1

This trench, 15 m long and 2.2 m deep, was excavated across the antislope scarp and depression controlled by the antithetic fault that defines the NW edge of the graben in its NE sector (Figs. 2, 8 and 9A). The trench, with a N130E orientation, was sited along a firebreak, SW of the headwall of a gully incised along the foot of the fault scarp. A few meters NE of the trench site the trough is affected by a fresh collapse sinkhole whose walls indicate the presence of a detrital deposit more than 1.5 m thick. The trench exposed a half-graben controlled by a single vertical fault with an associated extensional fissure (Figs. 8 and 9B). A total of six stratigraphic units were differentiated: (1) Bedrock: White limestone in beds 20–50 cm thick. (2) Regolith: Massive light brown silt with some scattered angular limestone clasts. Locally it grades into matrix-free angular limestone clasts. (3) Lower unit of graben fill: Massive and highly cohesive dark brown-grey clayey silt with scattered subangular limestone clasts, mostly less than 1 cm long. It shows abundant millimetre-size voids filled with white secondary carbonate. This massive unit is confined to the asymmetric depression created by the fault and fills the associated bottom fissure. A terrestrial snail (*Jaminia quadridens*; Müller, 1774) collected 15 cm below the top of this unit has yielded an age of 3572–3408 cal BP at 2 sigma (Table 1). (4) Upper unit of graben fill: Massive dark brown clayey silt with numerous scattered subangular limestone pebbles. Although the contact between units 3 and 4 was not obvious, it has been delineated with a reasonable level of confidence considering that unit 4 is much less cohesive and does not have white secondary carbonate. This unit partly overlaps the footwall scarp. An age range of 265–0 cal BP has been obtained from a piece of charcoal extracted 17 cm above the base of this unit. Units 3 and 4 correspond to a slope wash deposit accumulated in a poorly drained area most probably affected by sporadic flooding. (5) Dark grey-brown soil horizon 5 cm thick with buried vegetation at the top. (6) Man-made deposit consisting of loose brown clayey silt bulldozed over the trough during the opening of the firebreak.

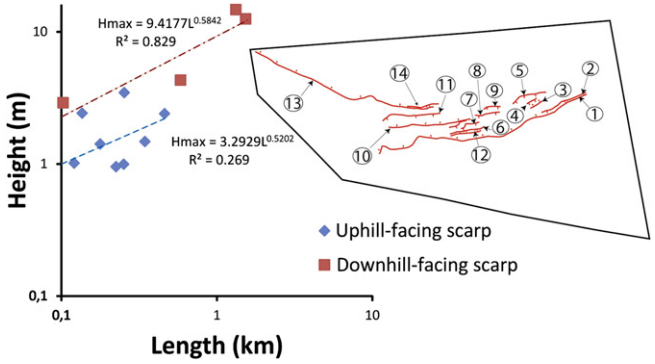

Fig. 7. Plot illustrating the relationship between the length of the fault scarps, measured as a straight line, and their maximum height (aspect ratio) in the crestal graben of the Rio Seco monocline. The upper and lower lines correspond to the power law regression for the downhill- and uphill-facing scarps, respectively. Inset depicts the mapped gravitational faults and their number.

The exposed half-graben is controlled by a subvertical fault with an associated tapering downwards fissure indicative of some horizontal separation. The bedrock is bent towards the fault on both blocks, dipping 40° in the hanging wall and 50–60° in the footwall (Figs. 8 and 9B). The flexure in the footwall may correspond to a drag fold, whereas downward bending of the strata in the downthrown block may be attributed to a roll-over anticline controlled by the underlying listric fault. In the adjacent West Stream the dip of this fault decreases downwards to 50° (Fig. 4). The density of fractures in the bedrock increases sharply towards the fault, grading into a dilated breccia of decimetre-size angular particles with the interclast spaces filled with dark grey clayey silt derived from the overlying deposits. The highest degree of fracturing occurs in the hinge zone of the footwall flexure. The top of the bedrock and the regolith show a vertical separation of 1.5 m in the trench. The actual vertical displacement on this fault is much higher as indicated by the 3.5 m high scarp situated a few meters to the SW (Fig. 9A). The lower part of unit 3 might be offset by the fault, as suggested by the reoriented fabrics of the clasts situated next to the fault. Clast reorientation could be also explained by downward ravelling through the fissure. The sharp and planar contact between unit 3 and the top of the tilted bedrock in the footwall dips 60° towards the trough. It seems to correspond to a bedding-controlled scarp face developed on fault-dragged bedrock and onlapped by unit 3 (free-face contact). Unit 4 overlaps the upper part of the fault-fold scarp and does not show any noticeable evidence of deformation.

The available numerical dates indicate that the depression associated with the antithetic fault scarp formed some time before 3.5 ka BP, most probably in the second half of the Holocene. A high sedimentation rate may be expected in this geomorphic setting. The height of the scarp (minimum vertical displacement) and the minimum age of the structure allow calculating an apparent vertical slip rate of 1 mm/yr. This apparent slip rate has not been calculated for closed slip cycles (closed-cycle slip rate) but with a cumulative vertical displacement divided by the known time span in which the displacement occurred, without knowing the number of cycles and the ratio of time in open vs. closed cycles (McCalpin, 2009c). The date obtained from unit 4 indicates that accumulation in historical times largely subdued the topography of the graben in this sector, favouring soil development. Unfortunately, the observed geometrical relationships do not allow us to elucidate whether the structure has formed progressively, episodically, or in a combined manner. A possible explanation is that a first faulting event older than 3.5 ka created a sediment trap at the foot of the antislope fault scarp, allowing the subsequent deposition of unit 3. A probable second faulting event deformed at least the lower part of unit 3 and created a fissure or widened a pre-existing one. However, the massive character of the deposits precludes the

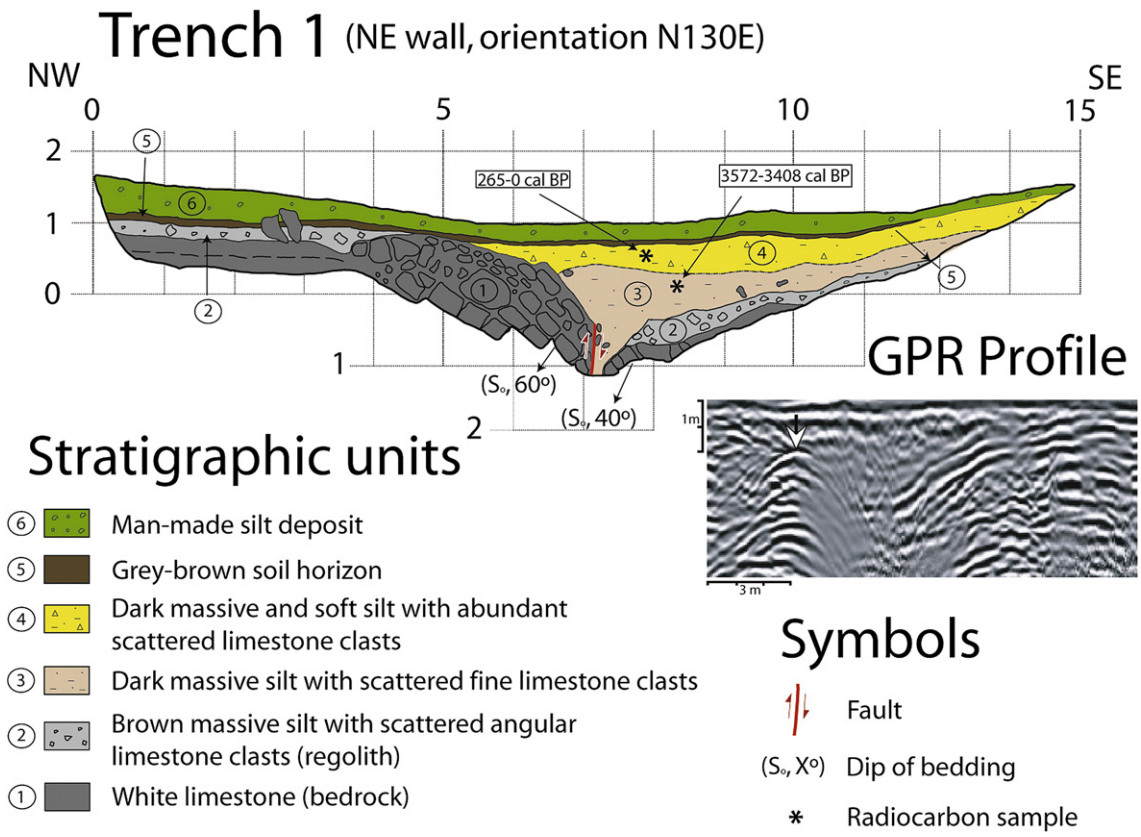

Fig. 8. Log of trench 1 and GPR profile acquired at this site. Arrow in GPR profile points to the fault plane. More extensive description of units in the text.

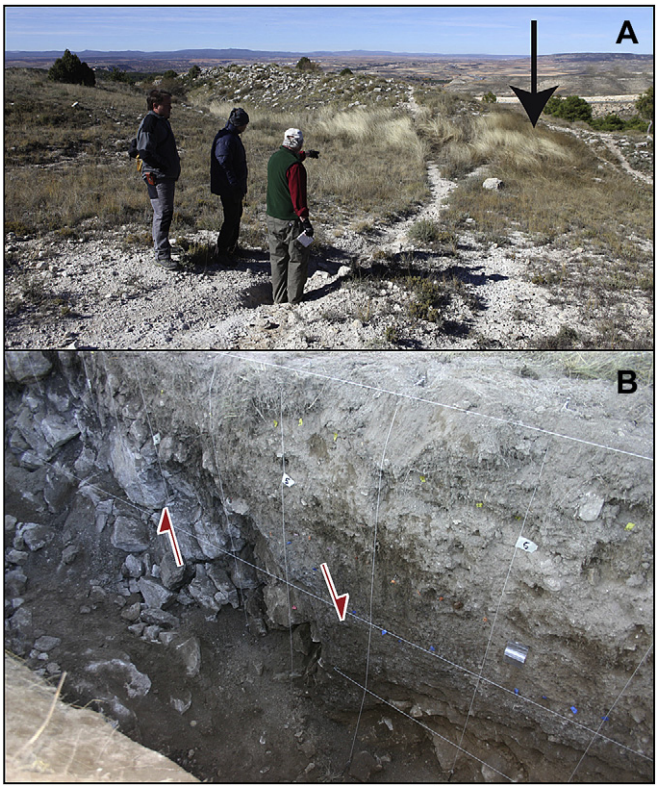

Fig. 9. A: Antislope scarp and depression investigated by trench 1. Arrow points to the trench site. B: North-eastern wall of trench 1, displaying a half-graben controlled by a single antithetic normal fault with an associated extensional fissure.

identification of angular unconformities. The lack of colluvial wedges could be explained by the formation of a low gradient bedrock scarp caused by the forward tilting of the strata (McCalpin, 2009b). An alternative explanation is that displacement on the fault, including the opening of the fissure and the folding of the bedrock, has occurred progressively. Potential cumulative wedge outs indicative of creep deformation are not observable in the massive graben deposits. Additionally, overlapping of the fault scarp by apparently undeformed deposits may be explained by rapid recent deposition of unit 4; that is, aggradation rate largely exceeds vertical displacement.

5.3. Trench 2

This trench was excavated with a N150E orientation in the central sector of a flat-bottomed depression associated with an antithetic fault scarp (Fig. 2). The trench, 16 m long and 2.3 m deep, covered the whole width of the trough, from the 0.5 m high antislope scarp situated at the NW margin to the steep slope forming the SE flank (Fig. 10). Bedrock, corresponding to limestone of the Miocene unit 2 of our map, was reached all along the trench. The excavation exposed a complex structure consisting of two asymmetric grabens separated by a horst in the central sector of the depression. The older stratigraphic units of the depression fill, some of them faulted, are confined to the grabens. The undeformed youngest unit veneers the whole depression truncating the underlying deformation structures. Some of the units mapped within the grabens have been correlated on the basis of facies resemblance. Unfortunately, datable material has only been found in the oldest unit of the SE graben, precluding the possibility of testing independently our correlation with numerical dates.

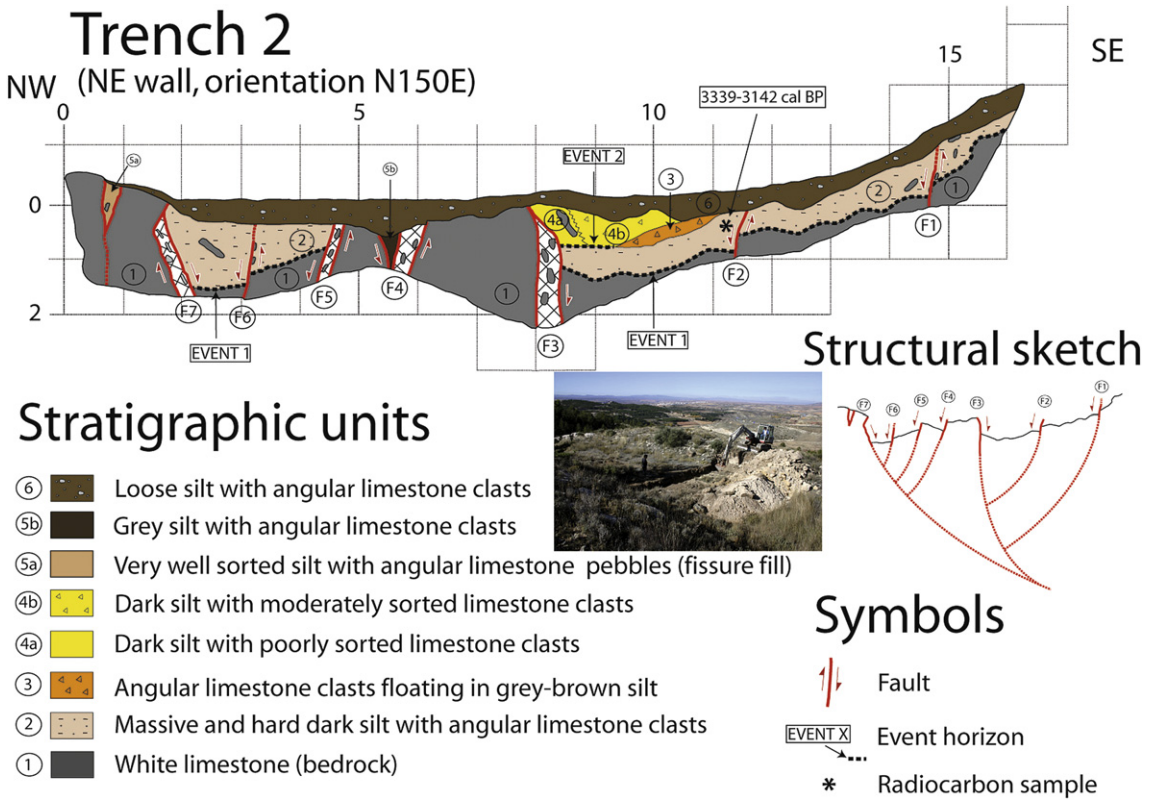

Fig. 10. Log of trench 2. More extensive description of units in the text. Inset photograph illustrates the geomorphic setting of the trench, excavated across a flat trough bounded by a steep bedrock slope and an uphill-facing limestone scarp.

The following units have been mapped in the trench: (1) Bedrock: Well-bedded white Miocene limestone, locally highly brecciated. (2) Massive and highly cohesive brown silt with angular limestone clasts and patches of secondary carbonate. The colour of this unit changes gradually from reddish brown beneath the SE slope into a greyish brown tone towards NW graben, indicative of more reducing conditions. The size of the clasts also decreases to the NW, whereas the sorting degree increases. Most likely, the upper part of the deposit situated between faults F6 and F7 corresponds to a different younger unit. However, its massive and homogeneous character has not allowed us to identify any clear stratigraphic discontinuity. This unit may be interpreted as colluvium that grades into a sheet wash deposit accumulated in the bottom of the poorly drained trough generated by surface faulting. A piece of wood 4 cm long collected at 25 cm above the base of unit 2, just NW of fault F2, has provided a calibrated age of 3339–3142 cal BP. (3) Massive poorly-sorted pebble- and cobble-sized angular limestone clasts with chaotic fabrics embedded in grey-brown silt. This lenticular unit 20 cm thick may correspond to a debris flow deposit derived from the SE slope. (4a) Loose dark grey-brown silt 65 cm thick with poorly sorted angular limestone clasts up to 50 cm long. Elongated clasts show rough fabrics dipping towards the SE. (4b) Massive dark grey-brown silt with abundant moderately sorted angular pebble- and cobble-sized limestone clasts with chaotic fabrics. Units 4a and 4b are correlative deposits separated by a gradational lateral facies change. These units are interpreted as proximal and distal facies of a colluvial wedge shed from a scarp produced by a displacement event on the underlying fault F3. Unit 4a truncates the shear zone (brecciated bedrock) of this fault resting on a free-face depositional contact. (5a) Fissure fill composed of well-sorted light grey silt with some angular limestone pebbles. Eolian deposition may have played a significant role in the infill this fissure, situated in an elevated ridge barely affected by runoff. (5b) Fissure fill consisting of angular limestone clasts embedded in loose grey clayey silt. (6) Loose massive light brown-grey silt with poorly sorted angular limestone clasts. The proportion and size of clasts increase towards the SE slope. This unit is interpreted as a young colluvium and sheet wash deposits.

The SE sector of the depression is underlain by a half-graben controlled by the down to the SE fault F3 (Fig. 10). This structure displays a 40 cm wide shear zone composed of brecciated limestone bedrock with subvertical fabrics. The breccia has large air-filled intergranular spaces indicative of dilation due to horizontal separation on the fault. Fault F3 affects unit 2 and is truncated by unit 4a. A minimum cumulative vertical offset of 1 m can be estimated on this fault using the top of the bedrock. Faults F1 and F2 are small throw secondary faults affecting unit 2, with around 20 and 30 cm of vertical separation, respectively. The trace of fault F1 was not clearly distinguishable in the massive unit 2. The NW graben is controlled by the SE-dipping fault F7 and the NW dipping faults F6 and F5, all of them offsetting unit 2. Faults F7 and F5 show shear zones in bedrock made up of dilated breccia with reoriented fabrics and open voids. Forward toppling of a bedrock block in the scarp associated with fault F7 has resulted in the opening of the 28 cm wide fissure filled by unit 5a and the oversteepening of the upper part of the fault plane. Neither a tilted block nor a fissure were observed in the opposite wall of the trench, where fault F7 showed a continuous plane with a 70SE dip. Faults F7 and F5 show minimum vertical separations of 200 cm and 40 cm, respectively, as measured on the top of the bedrock. Vertical throw in fault F6 is 20 cm. The bedrock horst situated between both grabens shows an NW dipping fault (F4) defined by a limestone breccia with an associated fissure filled by unit 5b. Bedding in the footwall of this fault shows an obvious drag fold. The overall structure exposed in

the trench may be interpreted as a complex half-graben controlled by a master fault (F7) with a keystone graben in the NW margin and a horst bounded by secondary synthetic and antithetic faults (see structural sketch of Fig. 10).

The structural and stratigraphic relationships observed in the trench may be explained by a minimum of two faulting events involving the development of multiple surface ruptures (Fig. 10). A first deformation event, occurred before 3.3–3.1 ka, created a small fault-angle depression bounded in the downhill side by an antislope scarp on the master fault F7. Unit 2 was deposited in this sediment trap. Probably, the formation of the horst started in the first faulting event, controlling a thickness reduction of unit 2 on this structure. A second faulting event younger than 3.3–3.1 ka deformed unit 2 (faults F1, F2, F3, F5, F6 and F7) and created the antislope scarp associated to fault F3. Erosion of this scarp led to the accumulation of the colluvial wedge corresponding to unit 4. Probably this second faulting event rejuvenated the scarp associated with fault F7 and created the fissure situated in the footwall. Thickness of unit 2 between faults F5 and F6 (80 cm) and that of unit 4 (65 cm) provide a minimum measure of the vertical displacement achieved in the first and second faulting events, respectively. The upper part of the massive deposit between faults F6 and F7 mapped as unit 2 most likely includes a younger unit deposited after the second faulting event. The vertical separation of the top of the bedrock across fault F7 (200 cm) provides a minimum estimate of the cumulative vertical displacement on the master fault, suggesting displacements per event higher than 1 m. Considering a minimum vertical displacement of 200 cm and a minimum age for the structure of 3.3 ka, we can obtain an apparent vertical slip rate of 0.6 mm/yr. The actual displacement and age values may be quite close to the used figures, considering that degradation of bedrock in the footwall must be slow and that the dated sample was obtained close to the base of the depression fill (25 cm), where a relatively high sedimentation rate may be expected.

5.4. Trench 3

This trench, 15.5 m long and 2.7 m deep, was excavated in a depression developed in a gully, upstream of an uphill-facing scarp perpendicular to the drainage (Fig. 2). The depression receives runoff and sediment supply from the main gully and a small tributary developed at the SW margin along the foot of the NE–SW trending fault scarp. The trench was excavated with a N140E orientation, roughly parallel to the main stream and perpendicular to the scarp. The NW edge of the trench was situated at the downstream margin of the depression fill and the SE termination was constrained by tree vegetation, precluding the exposure of bedrock.

Similarly to trench 2, the excavation exposed two grabens and a horst in between (Fig. 11). Three main groups of Holocene deposits were differentiated; faulted sediments associated with each of the grabens and a sedimentary package with no evidence of deformation that unconformably overlie the older units and truncates the underlying structures. Unlike trench 2, we were not able to establish an unambiguous correlation between the deposits associated with the two grabens due to the following reasons: (1) The sediments in each graben were derived from different provenances, but they are internally homogeneous within each graben. Faulted units in the SE graben come from the main drainage, whereas sediment supply in the NW graben comes mainly from the tributary gully. The horst probably disconnected the two depressions since an early stage. (2) Due to the difficulty of finding datable material, the chronology of the graben deposits is poorly constrained, precluding a reliable correlation on the basis of numerical dates. Consequently, we have

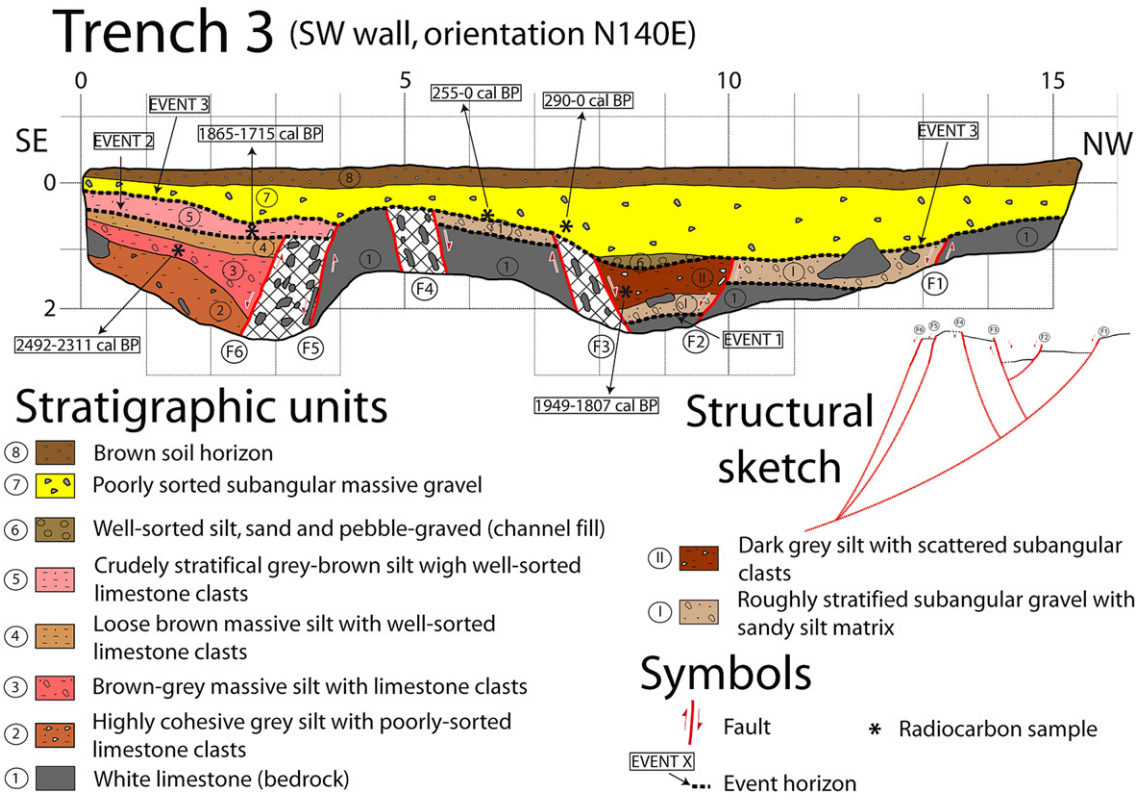

Fig. 11. Log of trench 3 excavated in a depression developed within a drainage upstream of an antislope scarp. More extensive description of units in the text. Due to lack of unambiguous correlation criteria, units of the SE and NW grabens are designated with Arabic and Roman numbers, respectively.

assigned Arabic numbers to the deposits of the SE graben and Roman numbers to sediments of the NW graben. The following units have been mapped: (1) Bedrock: Massive white limestone, locally highly brecciated. (2) Highly cohesive dark grey massive silt with scattered poorly sorted angular limestone clasts. Abundant bioturbation-related millimetre-sized pores filled with white secondary carbonate. Elongated clasts show a prevalent NW dip. (3) Brown-grey massive silt with scattered angular limestone clasts. This unit is softer and has less bioturbation and secondary carbonate than unit 2. A terrestrial snail obtained at 10 cm above the base of the unit has yielded an age of 2492- 2311 cal BP. (4) Loose light greyish brown massive silt with well-sorted granule- and pebble-sized subrounded limestone clasts. Some traces of bioturbation partly filled by secondary carbonate. (5) Crudely stratified grey-brown loose silt with abundant pebble-sized well-sorted subangular clasts. An age of 1865–1715 cal BP has been obtained from a terrestrial snail collected at 15 cm above the base of the unit. Units 2 to 5 may be interpreted as fluvial-palustrine facies deposited in a low-gradient and poorly-drained depression. (I) Highly cohesive, roughly stratified and moderately sorted subangular pebble-gravel with grey sandy silt matrix. This unit shows abundant bioturbation and secondary carbonate and contains some large limestone boulders. (II) Cohesive dark grey silt with scattered subangular pebble-sized clasts. A piece of charcoal collected 25 cm above the base of the unit has been dated at 1949–1807 cal BP. This age range overlaps that obtained from unit 5. Units I and II may be interpreted as interfingered fluvial and colluvial facies coming from the tributary gully and the adjacent antislope scarp. (6) Channel filled of stratified, well-sorted and loose silt, sand and pebble-gravel. The edge of the channel base truncates fault F3. (7) Poorly sorted and subangular massive pebble- and cobble-gravel with grey-brown silt matrix. The irregular base of this unit truncates the underlying faults. Charcoal pieces collected at and close to the base of this unit have been dated at 255–0 cal BP and 290–0 cal BP. This deposit most likely records sediment accumulation during storm-derived high competence flow events. (8) Brown soil horizon around 25 cm thick.

The SE sector of the trench exposed a half-graben controlled by the SE-dipping faults F6 and F5 (Fig. 11). Bedrock between both faults has been transformed into a 1.1 m wide loose breccia with shear fabrics. Fault F6 has deformed units 2, 3 and 4 and is truncated by unit 5. This latter unit has been offset by fault F5 (Fig. 12A). The thickness of units 2 to 4 (150 cm) provides a minimum estimate of the cumulative vertical displacement on fault F6. The minimum vertical offset on fault F5 is 45 cm, as measured using the top of the bedrock on both blocks. The NW graben is bounded by faults F4 and F1 and the greatest subsidence is reached in the inner block downthrown by faults F2 and F3 (Figs. 11 and 12B). The four faults offset unit I and faults F3 and F2 also displace unit II. Probably unit II has been eroded from the blocks flanking the inner graben. Faults F4 and F3 show well-defined shear zones in bedrock around 70 cm wide composed of dilated angular limestone clasts with reoriented fabrics. The top of bedrock provide a minimum cumulative vertical displacement in this graben of 175 cm. Like trench 2, the overall structure of trench 3 may be described as a complex half-graben with a horst separating a keystone graben to the NW and a half-graben to the SE.

The geometrical relationships observed in the SE half-graben can be explained by a minimum of 3 faulting events (Figs. 11 and 12A). A first surface rupture event before 2.5 ka created a poorly drained or closed depression within the stream in which units 2 to 4 were accumulated. In a second deformation event, occurred between 2.5 and 1.7 ka, units 2, 3 and 4 were offset by fault F6. The third and most recent event (MRE) is recoded by fault F5, which displaces unit 5 and is truncated by unit 7. The MRE occurred after 1865 cal BP. A maximum average recurrence interval of 1.25 ka can be estimated considering the two recentmost recorded events. It is important to note that this average recurrence has not been derived from closed-cycle data (McCalpin, 2009c). The minimum vertical throw of 195 cm in this half-graben with a minimum age of 2.5 ka indicates an apparent slip rate of the order of 0.8 mm/yr and an average displacement per event greater than 65 cm.

Fig. 12. A: Margin of half-graben exposed in the SE sector of trench 3, where upward truncation of two faults by different units record two faulting events. B: Graben in NW sector of trench 3 overlain unconformably by an undeformed deposits.

The stratigraphy and structure of the NW graben records a minimum of two faulting events (Figs. 2 and 12B). The first one occurred before 1.9 ka and created a sediment trap in which units I and II were deposited. This closed or poorly drained depression was probably controlled by an upslope-facing scarp associated with fault F1. In the second event, subsequent to 1949 yr BP, faults F1, F2, F3 and F4 offset units I and II. The minimum vertical throw of 175 cm in this half-graben, with a minimum age of 1950 yr BP, indicates an apparent slip rate of the order of 0.9 mm/yr and an average displacement per event greater than 87 cm if the two events interpretation is correct. The first event recorded in the two grabens could be contemporaneous and the penultimate and most recent events inferred in the SE graben may have also affected the NW graben, which probably records an underrepresented faulting sequence. The loosely bracketed age of the second event in the NW graben (<1950 yr BP) overlaps the age range ascribed to the penultimate and most recent events in the SE graben (2.5–1.7 ka and <1865 yr BP).

6. Discussion and conclusions

On the NW flank of Los Mansuetos mesa, passive bending of the Neogene formations due to interstratal dissolution of the

underlying Triassic evaporites has resulted in the development of a 1.7 km long monocline with a synform in the lower flexure. The Rio Seco valley flows concordantly down this gravitational syncline, which has 130 m of structural relief. The crest of the monocline is affected by a keystone graben of the same length with conspicuous topographic expression. In early publications the origin of the Rio Seco flexure was attributed to diapirism (Gautier et al., 1972; Moissenet, 1983; 1984). More recent and detailed studies argue that the downward displacement of the sediments is not consistent with diapiric processes, which would cause uplift, but with evaporite dissolution-induced subsidence (Gutiérrez, 1998; Calvo et al., 1999). The presented work improves the existing knowledge on the geology of the type section proposed for the definition of the Turolian, a Mediterranean Neogene continental stage, where most of the deformation structures have a nontectonic origin (Calvo et al., 1999).

The 130 m of structural relief in the Rio Seco syncline provides a measure of the cumulative subsidence magnitude and a minimum value for the thickness of evaporites removed by subsurface dissolution. Although gypsum is the only evaporitic lithology found in the outcrops of the M2 Middle Triassic unit, most probably a significant proportion of the gravitational deformation is related to dissolution of thick halite bodies. Borehole data indicate that this Middle Triassic unit may include up to 300 m of halite in the subsurface (Ortí et al., 1996). Two non-exclusive explanations may be proposed for the coincidence between the axis of the syncline and the path of the Rio Seco Creek: (1) Dissolution and subsidence has been more intense beneath a pre-existing drainage, which acted as the base level for discharging groundwater flows controlling the area of greatest dissolution. (2) Our preferred alternative is that the Rio Seco Creek has adapted its path to an actively subsiding trough generated by dissolution-induced sagging. Probably the development of the Rio Seco syncline and monocline started in the Late Pliocene, when the central sector of Teruel Graben changed from endorheic into exorheic conditions (Gutiérrez et al., 2008a). The development of a new incised drainage and the increase in hydraulic gradient induced a change in the pattern and rate of groundwater flow, favouring interstratal dissolution. Additionally, the new drainage allowed the evacuation of large volumes of dissolved evaporites.

The 1.7 km long keystone graben developed in the crest of the monocline is controlled by a master synthetic normal fault and a swarm of shorter antithetic and synthetic faults. This extensional structure counterbalances the shortening caused by sagging in the adjacent syncline. In fact, the width of the graben and the number of faults decreases towards the sector where the synform attenuates. Estimates of shortening and extension using cross-sections indicates that the shortening (up to ca. 20 m) is counterbalanced by dip-slip displacement on normal faults and horizontal separation on faults and fissures in the keystone graben, in agreement with the structures identified at the surface and exposed in trenches.

According to (Hanson et al., 1999; p. 3–31), collapse-related scarps typically have aspect ratios (H_{max}/L) higher than 10^{-3}. In the crestal keystone graben of the Rio Seco monocline, the downhill-facing scarps have an average aspect ratio of 0.029. The aspect ratios of the 8 uphill-facing scarps range from 0.004 to 0.017, with an average value of 0.008 (Table 2). If we consider the minimum cumulative vertical displacement (D) of 2 m and 1.95 m measured in trenches 2 and 3 dug across antislope scarps 121 and 178 m long, the relation D/L reaches 0.016 and 0.010, one order of magnitude higher than those for the aspect ratio of the antislope scarps. Dawers et al. (1993) analysed the scaling relation between fault displacement and length using data from a population of tectonic Quaternary normal faults located in the Volcanic Tableland, in northern Owens Valley, California. These faults span three orders of magnitude in length and form bedrock scarps on a dominantly flat surface with heights roughly equal to the vertical displacement (negligible erosion and aggradation in the upthrown and downthrown blocks, respectively). These faults, generated by a large number of displacement events, are characterised by Dmax/L ($\sim$Hmax/L) ratios of 10^{-2}, ranging from 0.009 to 0.020. A similar relation is found by Cowie and Scholz (1992) for short faults (<1 km) combining several data sets. According to the empirical relationships of Wells and Coopersmith (1994), the aspect ratio of single-event surface ruptures associated to normal fault earthquakes are of the order of 10^{-5}. The apparently low values obtained for the aspect ratio of the antislope fault scarps in the Rio Seco graben may be explained by two circumstances: (1) The height of the scarps decreases rapidly due to aggradation in the downthrown block, since the uphill-facing scarps act as traps for sediments. (2) The investigated fault scarps have been generated by a few displacement events (2 or 3), as revealed by the interpretation of the trenches. The data presented indicate that aspect ratios may be largely dependent not only on the origin of the fault scarps, but also on their orientation (uphill-facing vs. downhill-facing), whether the height of the scarps is modified by erosion and/or aggradation processes and whether the scarps result from single or multiple events. The aspect ratio of normal fault scarps tends to increase with age and the number of events (Dawers et al., 1993).

Three trenches were excavated in depressions associated with uphill-facing scarps. One of them exposed a half-graben whereas the other two a buried horst and graben structures. The overall structure of the latter may be interpreted as a half-graben with a keystone graben and a horst associated with the master fault. In the three trenches, the presence of fissures and highly dilated fault breccias with decimetre-sized voids indicate a significant horizontal separation component. The three investigated troughs are late Holocene in age, based on the AMS radiocarbon dates obtained from the samples collected closest to the base of the infill (3.5–3.4 ka in Trench 1, 3.3–3.1 ka in Trench 2 and 2.5–2.3 ka in Trench 3). Most probably, the actual age of the troughs is not much older than the available dates given the high sedimentation rates expected in these geomorphic contexts; steep slopes and a defeated drainage. Using the minimum cumulative vertical displacement measured at the trench sites and the minimum age of the depressions we have estimated apparent vertical slip rates ranging from 0.6 to 1 mm/yr. These values are significantly larger than the long-term vertical slip rates estimated for the tectonic normal faults in the Iberian Range (Gutiérrez et al., 2008a).

Hanson et al. (1999, p. 2–90) indicates that most dissolution-induced faults form continuously. However, the stratigraphical and structural relationships observed in trenches 2 and 3 reveal episodic displacement. Evidence of stepwise kinematics includes upward fault truncation, unconformities and colluvial wedges. Conversely, the geometrical relationships of trench 1 are ambiguous and could be explained alternatively by progressive and episodic displacement. The stick-slip kinematics of the investigated gravitational faults may be related to the functioning of the subsidence phenomena related to interstratal dissolution of evaporites. Two processes are involved: dissolution of evaporites and gravitational deformation of the overlying rocks. Although dissolution may operate in a continuous way, collapse may be discontinuous occurring when the voids created by karstification reach a critical size. Some external factors may accelerate or trigger dissolution and subsidence processes. The intensity of interstratal dissolution may increase during more humid periods due to enhanced groundwater recharge and flow. It may also augment during phases of downcutting of the drainage network, involving an increase in

the hydraulic gradient and favouring the deepening of the groundwater flows (karst system rejuvenation). The onset of the formation of the investigated structures appears to coincide with a more humid period identified in some Spanish and Mediterranean lake records. Cores from Montcortès lake (Eastern Pyrenees, NE Spain) and Zoñar Lake (Betic Cordillera, S Spain) indicate higher humidity for the period 3800-2350 cal yr BP (Corella et al., 2011) and after 3.5 ka (Martín-Puertas et al., 2008), respectively. Lacustrine terraces in the Bujaraloz playa-lakes (Ebro Basin, NE Spain) deposited between 3.9 and 2 ka record a period characterised by more positive hydrological balance that favoured aggradation and prevented eolian deflation (Gutiérrez et al., 2011).

Collapse events could be triggered by seismic shaking. Several lines of evidence reveal that the area has been affected by large magnitude earthquakes in the Pleistocene: (1) Different types of liquefaction structures attributed to earthquakes with magnitudes (m_b) between 5 and 7.5 have been documented close to Concud-Teruel Fault in the deposits of two Pleistocene terrace levels of the Alfambra River, situated at ca. 60 and 40 m above the current channel (Lafuente et al., 2008). (2) Evidence of multiple Late Pleistocene faulting events on the Concud Fault inferred from paleoseismological trenches (Lafuente et al., 2010a) and from an artificial exposure (Gutiérrez et al., 2008a; 2010; Lafuente et al., 2010b). Unfortunately, there are no data available on Holocene paleoearthquakes. No large magnitude earthquakes are included in the historical and instrumental catalogues. The largest historical earthquakes felt in the Teruel Graben correspond to the 1656 Ademuz (I_o VIII) and the 1828 Teruel (I_o IV-V) events, with epicentres located around 40 km south of Teruel and in Teruel city area, respectively (Mezcua and Martínez-Solares, 1983; Martínez-Solares and Mezcua, 2002). Estimated magnitudes (Mw) for these earthquakes are 5.75 and 3.45–4.0 applying the empirical relationship proposed by Rueda and Mezcua (2001), respectively. The largest earthquake recorded instrumentally in Teruel Graben corresponds to the 2006 Mb 4.3 Casas Bajas event, whose epicentre was located in the southern sector of the basin around 38 km south of Teruel city (IGN, 2011).

Although the investigated gravitational faults may have a stick-slip type of displacement like seismogenic faults, some parameters in addition to the high vertical slip rates support the nontectonic origin. The average recurrence of the faulting episodes, around 1.2–2 ka, is shorter than that for seismogenic faults in this intraplate area (Gutiérrez et al., 2009; 2010; Lafuente et al., 2010a; b). Additionally, the magnitude of the estimated displacement per event, higher than 65 cm, is too high for surface ruptures 121 and 178 m long. According to the empirical relationships of Wells and Coppersmith (1994), average displacements of 65 cm are expectable for normal fault surface ruptures around 28 km long.

Acknowledgements

This research work has been funded by the national project CGL2010-16775 (Ministerio de Ciencia e Innovación and FEDER) and a research grant of the Instituto de Estudios Turolenses. Authors would like to thank the Servicio Provincial de Medio Ambiente de Teruel for giving permission to excavate the trenches (document 72695) and to Drs. Belén Leránoz and Dr. Luis Alcalá for helping with the logistics of the investigation. Domingo Carbonel has a FPI grant of the Ministerio de Ciencia e Innovación. The authors are very grateful to the valuable work of the reviewers, Dr. Anthony H. Cooper (British Geological Survey), Mr. Robert Kirkham, and the editor Dr. Joao Hippertt.

References

Adrover, R., Mein, P., Moissenet, E., 1978. Nuevos datos sobre la edad de las formaciones continentales neógenas de los alrededores de Teruel. Estudios Geológicos 34, 205–214.

Aguirre, E., 1975. División estratigráfica del Neógeno continental. Estudios Geológicos 31, 587–595.

Aguirre, E., Alberdi, M.T., Pérez-González, A., 1975. Turolian. In: Steininger, F.F., Nevesskaya, L.A. (Eds.), Stratotypes of Mediterranean Neogene Stages, vol. 2. Veda Publ. Slovak Acad. Sci, Bratislava, pp. 149–152.

Alcalá, L., Alonso-Zarza, A.M., Álvarez Sierra, M.A., Azanza, B., Calvo, J.P., Cañaveras, J.C., van Dam, J.A., Garcés, M., Krijgsman, W., van der Meulen, A.J., Morales, J., Peláez-Campomanes, P., Pérez-González, A., Sánchez Moral, S., Sancho, R., Sanz-Rubio, E., 2000. El registro sedimentario y faunístico de las cuencas de Calatayud-Daroca y Teruel. Evolución paleoambiental y paleoclimática durante el Neógeno. Revista de la Sociedad Geológica de España 13, 323–343.

Alonso-Zarza, A.M., Calvo, J.P., 2000. Palustrine sedimentation in an episodically subsiding basin: the Miocene of the northern Teruel Graben (Spain). Paleogeography, Paleoclimatology, Paloeecology 160, 1–21.

Anadón, P., Moissenet, E., 1996. Neogene basins in the Eastern Iberian Range. In: Friend, P., Dabrio, C.J. (Eds.), Tertiary basins of Spain, the stratigraphic record of crustal kinematics. Cambridge University Press, Cambridge, pp. 68–76.

Anadón, P., Roca, E., 1996. Geological setting of the Tertiary basins of Northeast Spain. In: Friend, P., Dabrio, C.J. (Eds.), Tertiary basins of Spain, the stratigraphic record of crustal kinematics. Cambridge University Press, Cambridge, pp. 43–48.

Anderson, N.L., Knapp, R., 1993. An overview of some of the larger scale mechanisms of salt dissolution in Western Canada. Geophysics 58, 1375–1387.

Anderson, N.L., Brown, R.J., Hinds, R.C., 1988. Geophysical aspects of Wabamun salt distribution in southern Alberta. Canadian Journal of Exploration Geophysics 24, 166–178.

Anderson, N.L., Hopkins, J., Martínez, A., Knapp, R.W., Macfarlane, P.A., Watney, W.L., Black, R., 1994. Dissolution of bedded rock salt: a seismic profile across the active eastern margin of the Hutchinson salt member, central Kansas. Computers and Geosciences 20, 889–903.

Anderson, N.L., Hinds, R.C., 1997. Glacial loading and unloading: a possible cause of rock salt dissolution in the Western Canada Basin. Carbonates and Evaporites 12, 43–52.

Baars, D.L., 2000. Geology of Canyonlands National Park, Utah. In: Sprinkel, D.A., Chidsey, T.C., Anderson, P.B. (Eds.), Geology of Utah's Parks and Monuments, vol. 28. Utah Geological Association Publication, pp. 61–83.

Bachman, G.O., 1984. Regional geology of Ochoan evaporites, northern part of Delaware Basin. New Mexico Bureau of Mines and Mineral Resources. Circular 184, 22 (plus appendices).

Baumgardner Jr., R.W., Hoadley, A.D., Goldstein, A.G., 1982. Formation of the Wink Sink, a salt dissolution and collapse feature, Winkler County, Texas. Texas Bureau of Economic Geology Report of Investigations 114, 38.

Black, T.J., 1997. Evaporite karst of Northern Lower Michigan. Carbonates and Evaporites 12, 81–83.

Calvo, J.P., Alcalá, L., Alonso-Zarza, A.M., van Dam, J., Gutiérrez Santolalla, F., 1999. Estratigrafía y estructura del área de Los Mansuetos (Cuenca de Teruel). Precisiones papa la definición del estratotipo del Turoliense. Geogaceta 25, 55–58.

Capote, R., Muñoz, J.A., Simón, J.L., Liesa, C.L., Arlegui, L.E., 2002. Alpine tectonics I: the Alpine system north of the Betic Cordillera. In: Gibbons, W., Moreno, T. (Eds.), The Geology of Spain. The Geological Society. London, Special Publications, 367–400.

Cartwright, J.A., Trudgill, B.D., Mansfield, C.S., 1995. Fault growth by segment linkage: an explanation for scatter in maximum displacement and trace length data from the Canyonlands grabens of SE Utah. Journal of Structural Geology 17, 1319–1326.

Cater, F., 1970. Geology of the Salt Anticline Region in Southwestern Colorado. U.S. Geological Survey Professional Paper 637, 80.

Christiansen, E.A., 1967. Collapse Structures near Saskatoon, Saskatchewan, Canada. Canadian Journal of Earth Sciences 4, 757–767.

Christiansen, E.A., 1971. Geology of the Crater Lake collapse structure in the Southeastern Saskatchewan. Canadian Journal of Earth Sciences 8, 1505–1513.

Christiansen, E.A., Karl-Sauer, E., 2001. Stratigraphy and structure of a Late Wisconsinan salt collapse in the Saskatoon Low, south of Saskatoon, Saskatchewan, Canada: an update. Canada Journal of Earth Sciences 38, 1601–1613.

Clague, J.J., Evans, S.G., 1994. A gravitational origin for the Hell Creek 'fault', British Columbia: Current Research 1994-A. Geological Survey of Canada, 193–200.

Cooper, A.H., 2002. Halite karst geohazards (natural and man-made) in the United Kingdom. Environmental Geology 42, 505–512.

Corella, P., Moreno, A., Morellón, M., Rull, V., Giralt, S., Rico, M., Sanz-Pérez, A., Valero-Garcés, B., 2011. Sedimentary evolution and palaeohydrology of karstic, meromictic Montcortés Lake (Spanish Pre-Pyrenees) during the last 6,000 years. Journal of Paleolimnology DOI: 10.1007/s10933-010-9443-3.

Cowie, P.A., Scholz, C.H., 1992. Displacement-length scaling relationship for faults: data synthesis and discussion. Journal of Structural Geology 14, 1149–1156.

Crusafont, M., 1965. Observations à un travail de M. Freudenthal et P.Y. Sondaar sur des nouveauz gisements d'Hipparion d'Espagne. Proceedings of the Koninklijke Nederlandse Akademie Van Wetenschappen B. 68, 121–126.

Cutler, W.G., 1983. Stratigraphy and Sedimentology of the Upper Devonian Grosmont Formation, northern Alberta. Bulletin of Canadian Petroleum Geology 31, 282–325.
Dawers, N.H., Anders, M.H., Scholz, C.H., 1993. Growth of normal faults: Displacement-length scaling. Geology 21, 1107–1110.
De Mille, G., Shouldice, J.R., Nelson, H.W., 1964. Collapse structures related to evaporites of the Prairie Formation, Saskatchewan. Geological Society of America Bulletin 75, 307–316.
Doelling, H.H., 2000. Geology of Arches National Park, Grand County, Utah. In: Sprinkel, D.A., Chidsey, T.C., Anderson, P.B. (Eds.), Geology of Utah's Parks and Monuments, vol. 28. Utah Geological Association Publication, pp. 11–36.
Ertec Northwest, Inc, 1981. The origin(s) of uphill-facing scarps, North Cascade Range, Washington: unpublished report by Ertec Northwest, Inc., Seattle, WA submitted to Puget Sound Power and Light Co., Nov. 1981, report no. 81-513, 77 p.
Ford, D., Williams, P., 2007. Karst Hydrogeology and Geomorphology. Wiley, Chichester.
Gautier, F., Moissenet, E., Viallard, P., 1972. Contribution à l'étude stratigraphique et tectonique du fossé néogène de Teruel (Chaînes Ibériques, Espagne). Bulletin du Muséum National dHistoire Naturelle 77, 179–200.
Gracia, F.J., Gutiérrez, F., Gutiérrez, M., 2003. The Jiloca karst polje-tectonic graben (Iberian Range, NE Spain). Geomorphology 52, 215–231.
Gustavson, T.C., 1986. Geomorphic development of the Canadian River Valley, Texas Panhandle: An example of regional salt dissolution and subsidence. Geological Society of America Bulletin 97, 459–472.
Gutiérrez, F., 1996. Gypsum karstification induced subsidence: Effects on alluvial systems and derived geohazards (Calatayud Graben, Iberian Range, Spain). Geomorphology 16, 277–293.
Gutiérrez, F., 1998. Fenómenos de subsidencia por disolución de formaciones evaporíticas en las fosas neógenas de Teruel y Calatayud. Ph.D. thesis, University of Zaragoza.
Gutiérrez, F., 2004. Origin of the salt valleys in the Canyonlands section of the Colorado Plateau. Evaporite dissolution collapse versus tectonic subsidence. Geomorphology 57, 423–435.
Gutiérrez, F., Cooper, A.H.,Surface morphology of gypsum karst. In: Frumkin, A. (Ed.). Treatise on Geomorphology. Elsevier. In press.
Gutiérrez, F., Gutiérrez, M., Gracia, F.J., McCalpin, J.P., Lucha, P., Guerrero, J., 2008a. Plio-Quaternary extensional seismotectonics and drainage network development in the central sector of the Iberian Chain (NE Spain). Geomorphology 102, 21–42.
Gutiérrez, F., Ortuño, M., Lucha, P., Guerrero, J., Acosta, E., Coratza, P., Piacentini, D., Soldati, M., 2008b. Late Quaternary episodic displacement on a sackung scarp in the central Spanish Pyrenees. Secondary paleoseismic evidence? Geodinámica Acta 21, 187–202.
Gutiérrez, F., Masana, E., González, A., Guerrero, J., Lucha, P., McCalpin, J.P., 2009. Late Quaternary paleoseismic evidence on the Munébrega Half-graben fault (Iberian Range, Spain). International Journal of Earth Sciences 98, 1691–1703.
Gutiérrez, F., Lucha, P., Guerrero, J., Gutiérrez, M., Carbonel, D., 2010. Discussion on the article "Paleoseismological análisis of an intraplate extensional structure: the Concud fault (Iberian Chain, Eastern Spain)". International Journal of Earth Sciences DOI: 10.1007/s00531-011-0660-4.
Gutiérrez, F., Desir, G., Valero, B., González-Sampériz, P., Moreno, A., Morellón, M., Gutiérrez, M., Linares, R., Zarroca, M., Guerrero, J., Carbonel, D., Lucha, P., Bonachea, J., Roqué, C., 2011. Holocene evolution of playa lakes in the central sector of the Ebro Depression base don morpho-stratigraphic analyses of lacustrine terraces. In: Turu, V., Constante, A. (Eds.), XIII Reunión Nacional de Cuaternario. AEQUA. Andorra, pp. 71–74.
Hanson, K.L., Kelson, K.I., Angell, M.A., Lettis, W.R. (Eds.), 1999. Techniques for identifying faults and determining their origins. U.S. Nuclear Regulatory Commission, Washington, contract report NUREG/CR-5503, 186 pp. plus appendices.
Hernández, A., Anadón, P., 1985. Memoria y Mapa Geológico de España, E. 1:200.000. Teruel, vol. 47. IGME, Madrid.
Hill, C., 1996. Geology of the Delaware Basin, Guadalupe, Apache, and Glass Mountains, New Mexico and West Texas. Permian Basin Section-SEPM, Publication No. 96-39, 440 pp.
Hopkins, J.C., 1987. Contemporaneous subsidence and fluvial channel sedimentation: Upper Mannville C Pool, Berry Field, Lower Cretaceous of Alberta. The American Association of Petroleum Geologists Bulletin 71, 334–345.
Huntoon, P.W., 1982. The Meander anticline, Canyonlands, Utah: An unloading structure resulting from horizontal gliding on salt. Geological Society of America Bulletin 93, 941–950.
Huntoon, P.W., 1999. Field-Based identification of salt-related structures and their differentiation from tectonic structures. In: HansonK.L., KelsonK.I., AngellM.A., LettisW.R (Eds.), Techniques for identifying faults and determining their origins. U.S. Nuclear Regulatory Commission, Washington, contract report NUREG/CR-5503, 186 pp. plus appendices.
IGN, 2011. Servicio de Información Sísmica del Instituto Geográfico Nacional. http://www.ign.es/ign/layoutIn/sismoFormularioCatalogo.do.
James, N.P., Choquette, P.W. (Eds.), 1987. Paleokarst. Springer-Verlag, New York.
Kirkham, R.M., Streufert, R.K., Kunk, M.J., Budhan, J.R., Hudson, M.R., Perry Jr., W.J., 2002. Evaporite tectonism in the Lower Roaring Fork river valley, west-central Colorado. In: Kirkham, R.M., Scott, R.B., Judkins, T.W. (Eds.), Late Cenozoic evaporite tectonism and volcanism in west-central Colorado, vol. 366. Geological Society of America special paper, pp. 73–99.
Kozary, M.T., Dunlap, J.C., Humphrey, W.E., 1968. Incidence of saline deposits in geologic time. Geological Society of America special paper 88, 43–57.
Lafuente, P., Rodríguez-Pascua, M.A., Simón, J.L., Arlegui, L.E., Liesa, C., 2008. Sismitas en depósitos pliocenos y pleaistocenos de la fosa de Teruel. Revista de la Sociedad geológica de España 21, 133–149.
Lafuente, P., Arlegui, L.E., Liesa, C., Simón, J.L., 2010a. Nuevo estudio paleosismológico en el sector central de la Falla de Concud (Fosa del Jiloca, Teruel): Resultados preliminares. In: Insua-Arévalo, J.M., Martín-González, F. (Eds.), Contribución de la Geología al análsisi de la peligrosidad sísmica. First Iberian Meeting on Active Faults and Plaeoseismology, Sigüenza, pp. 67–70.
Lafuente, P., Arlegui, L.E., Liesa, C.L., Simón, J.L., 2010b. Paleoseismological analysis of an intraplate extensional structure: the Concud fault (Iberian Chain, Eastern Spain). International Journal of Earth Sciences doi: 10.1007/s00531-010-0542-1.
Maley, V.C., Huffington, R.M., 1953. Cenozoic fill and evaporite solution in the Delaware Basin, Texas and New Mexico. Geological Society of America Bulletin 64, 539–546.
Marks, P., 1971. Turolian. Giornale de Geologia 37, 209–213.
Martín-Puertas, C., Valero-Garcés, B., Mata, P., González-Sampériz, P., Bao, R., Moreno, A., Stefanova, V., 2008. Arid and humid phases in southern Spain during the last 4000 years: The Zoñar Lake record, Córdoba. Holocene 18, 907–921.
Martínez Solares, J.M., Mezcua, J., 2002. Catálogo sísmico de la Península Ibérica (880 a.C. – 1900). Monografía 18. Instituto Geográfico Nacional, Madrid.
McCalpin, J.P., 2009a. Field techniques in Paleoseismology. Terrestrial environments. In: McCalpin, J.P. (Ed.), Paleoseismology. Academic Press, San Diego, pp. 29–118.
McCalpin, J.P., 2009b. Paleoseismology in extensional tectonic environments. In: McCalpin, J.P. (Ed.), Paleoseismology. Academic Press, San Diego, pp. 171–269.
McCalpin, J.P., 2009c. Application of Paleoseismic Data to Seismic Hazard Assessment and Neotectonic Research. Available at. In: McCalpin, J.P. (Ed.), Paleoseismology. Academic Press, San Diego. http://www.elsevierdirect.com/companions/9780123735768 :
McCalpin, J.P., Irvine, J.R., 1995. Sackungen at the Aspen Highlands ski area, Pitkin County, Colorado. Environmental and Engineering Geoscience 1, 277–290.
McCleary, J., Dohrenwend, J., Cluff, L., Hanson, K., 1978. 1872 earthquake studies, Washington Public Power Supply System Nuclear Project Nos. 1 and 4: unpublished report by Woodward-Clyde Consultants, San Francisco, CA submitted to United Engineers and Constructors, Inc. April 1978, contract No. 52028, 75 p. (plus appendices).
McGill, G.E., Stormquist, A.W., 1979. The Grabens of Canyonlands National Park, Utah: Geometry, Mechanics, and Kinematics. Journal of Geophysical Research 84 (B9), 4547–4563.
Mein, P., 1990. Updating of MN Zones. In: Lindsay, E.H. (Ed.), European Neogene Mammal Chronology. Plenum Press, New York, pp. 73–90.
Mein, P., Moissenet, E., Adrover, R., 1989–1990. Biostratigraphie du Néogène supérieur du bassin de Teruel. Paleontologia i Evolució 23, 121–139.
Meléndez, A., Aurell, M., Badenas, B., Soria, A.R., 1995. Las rampas carbonatadas del Triásico medio en el sector central de la Cordillera Ibérica. Cuadernos de Geología Ibérica 19, 173–199.
Memesh, A., Dini, S., Gutiérrez, F., Wallace, C.A., 2008. Evidence of large-scale subsidence caused by interstratal karstification of evaporites in the Interior Homocline of Central Saudi Arabia European Geosciences Union General Assembly. Geophysical Research Abstracts, vol. 10, A-02276.
Mezcua, J., Martínez Solares, J.M., 1983. Sismicidad en el área Ibero-Magrebí. Instituto Geográfico Nacional, Madrid. Pub. 203, 299 p.
Moissenet, E., 1983. Aspectos de la Neotectónica en la Fosa de Teruel. Geología de España. IGME vol. II, 423–446.
Moissenet, E., 1984. Lévolution tectonique du fossé de Teruel (Chaînes Ibériques orientales, provinces de Cuenca, Teruel et Valence, Espagne), vol. 299. Comptes Rendus de l'Academie des Sciences Paris. Serie II, 4, 173–178.
Moore, J.M., Schultz, R.A., 1999. Processes of faulting in jointed rocks of Canyonlands National Park, Utah. Geological Society of America Bulletin 111, 808–822.
Neal, J.T., Colpitts, R.M., 1997. Richard Lake, an evaporite karst depression in the Holbrook Basin, Arizona. Carbonates and Evaporites 12, 91–98.
Olive, W.W., 1957. Solution-subsidence troughs, Castile Formation of Gypsum Plain, Texas and New Mexico. Bulletin of the Geological Society of America 68, 351–358.
Ortí, F., García-Veigas, J., Rosell, L., Jurado, M.J., Utrilla, R., 1996. Formaciones salinas de las cuencas triásicas en la Península Ibérica: caracterización petrológica y geoquímica. Cuadernos de Geología Ibérica 20, 13–35.
Powers, R.W., Ramirez, L.F., Redmond, C.D., Elberg Jr., E.L., 1966. Geology of the Arabian Peninsula; Sedimentary geology of Saudi Arabia. U.S. Geological Survey Professional Paper 560-D, 147.
Reimer, P.J., Baillie, M.G.L., Bard, E., Bayliss, A., Beck, J.W., Bertrand, C., Blackwell, P.G., Buck, C.E., Burr, G., Cutler, K.B., Damon, P.E., Edwards, R.L., Fairbanks, R.G., Friedrich, M., Guilderson, T.P., Hughen, K.A., Kromer, B., McCormac, F.G., Manning, S., Bronk Ramsey, C., Reimer, R.W., Remmele, S., Southon, J.R., Stuiver, M., Talamo, S., Taylor, F.W., van der Plicht, J., Weyhenmeyer, C.E., 2009. IntCal09 and Marine09 radiocarbon age calibration curves, 0-50,000 years cal BP. Radiocarbon 51, 1111–1150.
Riba, O., 1991. Estratigrafía del Pérmico y Triásico. In: Gutiérrez, M., Melendez, A. (Eds.), Introducción a la Geología de la Provincia de Teruel. Teruel, pp. 35–54.
Rosen, M.R., 1994. The importance of groundwater in playas: A review of playa classifications and the sedimentology and hydrology of playas. In: Rose, M.R.

(Ed.), Paleoclimate and Basin Evolution of Playa Systems, vol. 289. Geological Society of America, pp. 1–18. special paper.
Rueda, J., Mezcua, J., 2001. Sismicidad, sismotectónica y peligrosidad sísmica en Galicia, vol. 35. Instituto Geográfico Nacional, Pub, Madrid.
Special Publication. In: Sasowsky, I.D., Feazel, Ch.T., Mylroie, J.E., Palmer, A.N., Palmer, M.V. (Eds.), Karst from recent to reservoirs, vol. 14. Karst Waters Institute. Leesburg, Virginia, p. 221.
Simón, J.L., 1989. Late Cenozoic stress field and fracturing in the Iberian Chain and Ebro Basin (Spain). Journal of Structural Geology 11, 285–294.
Stanton, R.J., 1966. The solution brecciation process. Geological Society of America Bulletin 77, 843–848.
Supajanya, T., Friederich, M.C., 1992. Salt tectonics of the Sakon Nakhon Basin, norhteastern Thailand. Seventh regional conference on Geology, mineral and hydrocarbon resources of Southeast Asia (GEOSEA VII), 1991.
Trudgill, B., 2002. Structural controls on drainage development in the Canyonlands grabens of southeast Utah. AAPG Bulletin 86, 1095–1112.
Utrilla, R., Pierre, C., Ortí, F., Pueyo, J.J., 1992. Oxygen and sulphur isotope compositions as indicators of the origin of Mesozoic and Cenozoic evaporites from Spain. Chemical Geology (Isotope Geoscience Section) 102, 229–244.
Walsh, J.J., Watterson, J., 1988. Analysis of the relationship between displacements and dimensions of faults. Journal of Structural Geology 10, 239–247.
Walters, R.F., 1978. Land Subsidence in Central Kansas Related to Salt Dissolution, vol. 214. University of Kansas Publications. Bulletin, 82 pp.
Warren, J.K., 1997. Evaporites, brines and base metals: fluids, flow and 'the evaporate that was'. Australian Journal of Earth Sciences 44, 149–183.
Warren, J.K., 2006. Evaporites. Sediments, Resources and Hydrocarbons. Springer, Berlin.
Wells, D.L., Coppersmith, K.J., 1994. New empirical relationships among magnitude, rupture length, rupture width, rupture area and surface displacement. Bulletin of the Seismological Society of America 84, 974–1002.
Yechieli, Y., Wood, W.W., 2002. Hydrogeologic processes in saline systems: playas, sebkhas, and saline lakes. Earth-Science Reviews 58, 343–365.